Supplementary Information for:

Toward E-Selective Olefin Metathesis: Computational Design and Experimental Realization of Ruthenium Thio-Indolate Catalysts

Immanuel Reim[1], Giovanni Occhipinti[1], Karl W. Törnroos[1], Deryn E. Fogg[1,2], Vidar R. Jensen[1,]*

[1]Department of Chemistry, University of Bergen, Allégaten 41, N-5007 Bergen, Norway

[2]Centre for Catalysis Research & Innovation, Chemistry Department, University of Ottawa, Ottawa, Ontario, Canada K1N 6N5

Table of Contents

S1. Experimental Procedures and Additional Experimental Results

General Procedures.

Reactions were carried out in an argon-filled glovebox at room temperature (25 ±2 °C), unless otherwise indicated. Solvents were dried and degassed using a Glass Contour solvent purification system, then stored under argon in the glovebox over 4 Å molecular sieves for at least 16 h prior to use, unless otherwise indicated. Liquid reagents were degassed by five consecutive freeze/pump/thaw cycles, and then stored under argon in the glovebox freezer (-35 °C)., Triisopropylsilanethiol, tetrakis(triphenylphosphine)-palladium(0), allybenzene, styrene, pyridine, potassium hydride, tetrabutylammonium fluoride and propene were obtained from Sigma Aldrich. Tricyclohexylphosphine[4,5-dimethyl-1,3-bis(2,4,6-trimethylphenyl)imidazol-2-ylidene][2-thienylmethylene] ruthenium(II) dichloride (catMETium® RF3) was kindly supplied by Evonik Industries. 7-Bromo-1H-indole and 2-Methyl-7-Bromo-1H-indole were obtained from Enamine. 2-Phenyl-7-Thiol-1H-indole was purchased from Santai Lab. NMR spectra were recorded on Bruker Biospin AV500 and 850 Ascend spectrometers at 298 K, and referenced against the residual proton signals of the deuterated solvents (^{1}H) [1]. HRMS ESI mass spectra were recorded by means of an orthogonal electron spray ionization ion source (ESI) interfaced to a JMS-T100LC AccuTOF mass spectrometer from JEOL USA, Inc. (Peabody, MA). The ions were transported into the orthogonal accelerating time-of-flight (TOF) single-stage reflectron mass analyzer by a high-frequency and high-voltage quadrupole ion guide. Detection was achieved with a dual microchannel plate detector. Elemental analyses were performed using an Elementar Vario EL III analyzer. GC quantification was performed on an Agilent 7890A series GC equipped with a flame ionization detector (FID), an Agilent 7683B series autosampler, and an Agilent HP-5 polysiloxane column (30 m length, 320 μm diameter). Calibration curves (peak areas vs. concentration for solutions with ca. 1:1 w/w decane/analyte) in the relevant concentration regimes were constructed using commercial samples (styrene, *trans*-stilbene, allylbenzene) [2]. Yields in catalytic runs were determined from the integrated peak areas (referenced against decane), compared to the substrate/decane ratio at time zero (t_0). GC samples were quenched using ca. 10 equiv of potassium tris(pyrazolyl)borohydride [3] in THF prior to analysis. Suitable crystals for diffraction experiments were immersed in Paratone-N (Hampton Research) in a nylon loop. Data collection was done on a Bruker AXS TXS rotating anode system with an APEXII Pt^{135} CCD detector using graphite-monochromated Mo Kα radiation (λ = 0.71073 Å).

Synthesis of 7-((triisopropylsilyl)thio)-1H-indole (L2a)

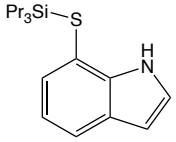

In a glovebox, a Schlenk finger was charged with 88 mg (2.2 mmol, 1.1 eq) KH in 10 mL of toluene. 457 µL (2.4 mmol, 1.2 eq) triisopropylsilanethiol was added to the suspension at once and the reaction was stirred for 30 minutes to form a colorless solution. 392 mg (2 mmol, 1 eq.) 7-Bromoindole in 10 mL of toluene and 231 mg (0.2 mmol, 0.1 eq) tetrakis(triphenylphosphine)-palladium(0) was added to the flask. The solution was then taken out of the glovebox and heated for 14 h at 120 ºC. After cooling the reaction to room temperature, the reaction mixture was filtered through a plug of SiO_2 with DCM as eluent. After removal of the solvent, the reaction was filtered through SiO_2 with hexane as eluent. After the removal of the solvent, the residual was taken up in THF and 50 mg Merrifield-Resin was added to the flask to remove residual triphenylphosphine. After 15 h the suspension was filtered over silica gel, the filtrate concentrated and purified via flash chromatography (SiO_2, 1:5 DCM:Hexane) to deliver the product as a colorless oil.

Yield: 420 mg (69 %)

^{1}H NMR (400 MHz, $CDCl_3$) δ 8.57 (s, 1H), 7.51 (dt, *J* = 7.9, 0.9 Hz, 1H), 7.29 – 7.20 (m, 2H), 6.98 (dd, *J* = 7.9, 7.4 Hz, 1H), 6.53 (dd, *J* = 3.2, 2.2 Hz, 1H), 1.33 – 1.14 (m, 3H), 1.02 (d, *J* = 7.4 Hz, 18H).

^{13}C-NMR ($CDCl_3$, 300 MHz): 139.0, 128.7 127.5, 124.0, 120.2, 119.7, 112.4, 103.2, 18.4, 13.3.

Synthesis of 2-methyl-7-((triisopropylsilyl)thio)-1*H*-indole (L2b)

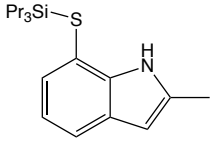

In a glovebox, a Schlenk finger was charged with 66 mg (1.65 mmol, 1.1 eq) KH in 7.5 mL of toluene. 386 µL (1.8 mmol, 1.2 eq) triisopropylsilanethiol was added to the suspension at once and the reaction was stirred for 30 minutes to form a colorless solution. 214 µL (1.5 mmol, 1 eq.) 2-Methyl-7-Bromo-1H-indole in 7.5 mL of toluene and 173.3 mg (0.15 mmol, 0.1 eq) tetrakis(triphenylphosphine)-palladium(0) was added to the flask. The solution was then taken out of the glovebox and heated for 14 h at 120 ºC. After cooling the reaction to room temperature, the reaction mixture was filtered through a plug of SiO2 with DCM as eluent. After removal of the solvent, the reaction was filtered through SiO2 with hexane as eluent. After the removal of the solvent, the residual was taken up in THF and 20 mg Merrifield-Resin was added to the flask to remove residual triphenylphosphine. After 15 h the suspension was filtered over silica gel, the solvent removed, and the resulting colorless solid used without further purification.

Yield: 291 mg (61%)

^{1}H NMR (300 MHz, $CDCl_3$) δ 8.27 (s, 1H), 7.38 (dt, *J* = 7.8, 0.9 Hz, 1H), 7.18 (dd, *J* = 7.5, 1.0 Hz, 1H), 6.93 (dd, *J* = 7.8, 7.4 Hz, 1H), 6.20 (dd, *J* = 2.4, 1.1 Hz, 1H), 2.47 (d, *J* = 0.6 Hz, 3H), 1.38 – 1.12 (m, 3H), 1.12 – 0.80 (m, 18H).

Synthesis of 2-H-7-Thio-1*H*-indole (L3a)

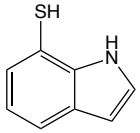

A Schlenk finger was charged with 427 mg (1.4 mmol, 1 eq) of **L2a** and 14.5 mL of THF and cooled to 0 °C. To this solution 2.8 mL (2.8 mmol, 2 eq) of 1 M tert-butylammonium fluoride solution was added and the solution was stirred for 1 h at 0 °C and then warmed up to rt and stirred for additional 30 min. The solution was cooled to 0 °C and 15 mL of 3 M HCl solution was added. The organic phase was separated, and the aqueous phase was extracted 3x with DCM. The combined organic phase was dried over $MgSO_4$ and concentrated under removed reduced pressure. The residual oil was purified via flash chromatography (SiO_2, 2:3 DCM:hexane), yielding the desired product as yellow solid.

Yield: 92 mg (44 %)

^{1}H NMR (400 MHz, $CDCl_3$) δ 8.44 (s, 1H), 7.59 (dq, *J* = 7.9, 0.9 Hz, 1H), 7.34 – 7.25 (m, 2H), 7.10 – 7.01 (m, 1H), 6.60 (dd, *J* = 3.2, 2.1 Hz, 1H), 3.28 (s, 1H).
^{13}C NMR (101 MHz, $CDCl_3$) δ 137.42, 127.88, 127.54, 124.46, 120.71, 120.37, 108.99, 103.62.
HRMS(ESI$^-$) m/z: $[M-H]^-$ Calcd for C_8H_6NS 148.0221; Found 148.0218.

Synthesis of 2-Methyl-7-Thio-1*H*-indole (L3b)

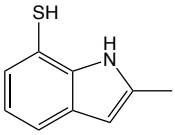

A Schlenk finger was charged with 287 mg (0.85 mmol, 1 eq) of **1b**, 2.8 mL of THF and 2.8 mL of Ethanol. To this solution 0.28 mL concentrated HCl (3.4 mmol, 4 eq) was added and the solution was stirred for 5 h. Afterwards, the solvents were removed under reduced pressure, re-dissolved in 2 mL of DCM. To the DCM solution 10 mL of hexane was added and the suspension was filtered through a plug of SiO_2 to remove the formed red solid. The solvent of the filtrated was removed under reduced pressure to yield the desired product as a colorless oil.
Yield: 90 mg (61 %)
^{1}H NMR (400 MHz, $CDCl_3$) δ 8.13 (s, 1H), 7.46 (dt, *J* = 7.9, 0.9 Hz, 1H), 7.22 (dt, *J* = 7.4, 1.0 Hz, 1H), 7.05 – 6.96 (m, 1H), 6.26 (dq, *J* = 2.1, 1.0 Hz, 1H), 3.25 (d, *J* = 1.0 Hz, 1H), 2.48 (d, *J* = 1.0 Hz, 3H).
^{13}C NMR (101 MHz, $CDCl_3$) δ 137.64, 135.54, 129.05, 126.48, 120.20, 119.59, 107.85, 101.37, 13.75.
HRMS(ESI$^-$) m/z: $[M-H]^-$ Calcd for C_9H_8NS 162.03774; Found 162.03750.
Elemental Analysis, calculated for C_9H_9NS: C, 66.22, H, 5.56, N, 8.58; found: C, 65.80, H, 5.33, N, 8.34.

Synthesis of potassium 7-sulfidoindol-1-ide (L4a)

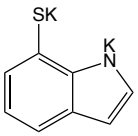

To 31.3 mg (0.21 mmol, 1 eq) L3a in 4 mL THF was 17.6 mg (0.44 mmol, 2.1 eq) KH added. Upon addition of KH, hydrogen was formed and the solution turned into a pink suspension. The reaction mixture was stirred for 14 h. The resulting pink suspension was filtered and the solid was washed with hexane (2x 5 mL) and dried. The dried compound indicates a quantitative conversion, measured by weight, and was used without further purification.

Synthesis of potassium 2-methyl-7-sulfidoindol-1-ide (L4b)

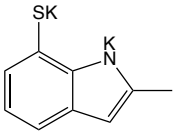

To 101 mg (0.6 mmol, 1 eq) **2b** in 4 mL THF was 52.1 mg (1.3 mmol, 2.1 eq) KH added. Upon addition of KH, hydrogen was formed and the solution turned into a pink suspension. The reaction mixture was stirred for 14 h. The resulting pink suspension was filtered and the solid was washed with hexane (2x 5 mL) and dried. The dried compound indicates a quantitative conversion, measured by weight, and was used without further purification.

Synthesis of potassium 2-phenyl-7-sulfidoindol-1-ide (L4c)

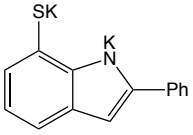

To 45 mg (0.2 mmol, 1 eq) of 2-Phenyl-7-Thio-1H-indole in 4 mL THF was 16.8 mg (0.42 mmol, 2.1 eq) KH added and the reaction mixture was stirred for 14 h to form a yellow solution. The solvent was removed under reduced pressure. The dried compound indicates a quantitative conversion, measured by weight, and was used without further purification.

Synthesis of Complex Ru20

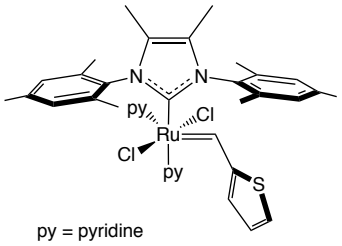

The synthesis was performed after a literature known procedure [4]. In a glovebox, a 25 mL vial, equipped with a magnetic stirring bar and a screw cap, was charged with complex tricyclohexylphosphine[4,5-dimethyl-1,3-bis(2,4,6-trimethylphenyl)imidazole-2-ylidene][2-thienylmethylene] ruthenium(II) dichloride (1087 mg, 1.234 mmol) and pyridine (4 mL). The vial was closed and the mixture stirred at room temperature for 1 hour. Then pentane (5 mL) was added to the reaction mixture causing the precipitation of a green solid. The solid was allowed to sediment (settle out) and then was isolated by vacuum filtration through a frit, washed three times with 5 mL of pentane and dried in the glovebox to give a green microcrystalline solid. Yield: 786 mg (84 % of yield).

The ^{1}H NMR is consistent with literature [4].

^{1}H NMR (500 MHz, C_6D_6) δ 18.94 (s, 1H), 8.79 (s, 2H), 8.62 – 8.57 (m, 2H), 7.74 (s, 1H), 7.40 (dt, *J* = 4.9, 1.1 Hz, 1H), 7.13 (s, 1H), 6.91 (t, *J* = 7.7 Hz, 1H), 6.74 (s, 5H), 6.59 (t, *J* = 6.3 Hz, 2H), 6.50 (dd, *J* = 5.0, 3.8 Hz, 1H), 6.42 (t, *J* = 7.7 Hz, 1H), 6.15 (t, *J* = 6.8 Hz, 2H), 2.64 (s, 6H), 2.33 (s, 6H), 2.14 (s, 6H), 1.54 (s, 6H)

Synthesis of Complex Ru21a/Ru21a'

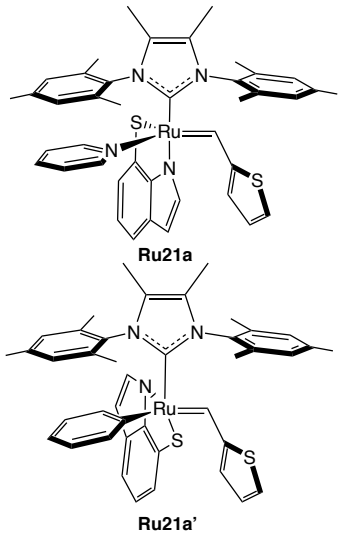

In a glovebox, a 20 mL vial was charged with 49.8 mg (0.68 mmol, 1 eq) of **Ru20** in 10 mL THF and 16.8 mg (0.075 mmol, 1.1) of **L4a** was added to the solution. A color change from green to red was observed immediately. After 30 min the reaction was completed, and the solvent removed under reduced pressure. The crude reaction mixture was redissolved in toluene, filtered through a pad of Celite and concentrated to about 2 mL. To this solution 10 mL hexane was added and cooled to -20 ºC for 15 h. The resulting microcrystalline solid was collected and washed with cold pentane (2 x 4 mL) to yield the desired product as brown/red solid. The ^{1}H NMR analysis shows the presence of two isomeric complexes **Ru21a** and **Ru21a'** in the ratio 95:5.

Yield: 31.1 mg (62 %)

Ru21a: ^{1}H NMR (850 MHz, C_6D_6) δ 16.21 (s, 1H), 8.12 (dd, *J* = 7.3, 0.9 Hz, 1H), 7.80 (dd, *J* = 7.6, 0.9 Hz, 1H), 7.53 (t, *J* = 7.4 Hz, 1H), 6.94 (dt, *J* = 4.9, 1.0 Hz, 1H), 6.76 – 6.72 (m, 2H), 6.53 (s, 2H), 6.44 (dd, *J* = 3.9, 1.2 Hz, 1H), 6.29 (d, *J* = 2.1 Hz, 2H), 6.26 – 6.19 (m, 4H), 5.94 (d, *J* = 2.6 Hz, 1H), 2.42 (s, 6H), 1.98 (s, 6H), 1.69 (s, 6H), 1.36 (s, 6H).

^{13}C-NMR (C_6D_6, 850 MHz): 263.2, 181.5, 152.5, 149.2, 148.2, 140.4, 138.3, 1338, 129.0, 126.5, 126.2, 123.6, 123.0, 122.5, 119.8, 117.7, 114.2, 105.0, 31.6, 20.7, 19.5, 8.7

Ru21a': ^{1}H NMR (850 MHz, C_6D_6) δ 15.38 (s, 1H), 8.71 (dt, *J* = 5.0, 1.5 Hz, 2H), 7.96 (dd, *J* = 7.7, 0.9 Hz, 1H), 7.86 (d, *J* = 7.0 Hz, 1H), 7.46 (t, *J* = 7.3 Hz, 1H), 7.25 (t, *J* = 1.2 Hz, 2H), 7.10 – 7.00 (m, 4H), 6.91 – 6.87 (m, 2H), 6.66 (tt, *J* = 7.4, 1.5 Hz, 1H), 6.28 – 6.27 (m, 2H), 5.84 (dd, *J* = 17.9, 12.1 Hz, 1H), 2.42 (s, 6H), 1.98 (s, 6H), 1.69 (s, 6H), 1.36 (s, 6H).

HRMS(ESI$^+$) m/z: $[M\text{-}NC_5H_5]^+$ Calcd for $C_{36}H_{36}N_3RuS_2$ 676.1394; Found 676.9120.

Synthesis of Complex Ru21b

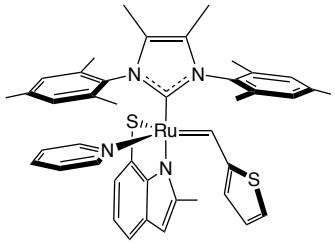

In a glovebox, a 20 mL vial was charged with 36.6 mg (0.05 mmol, 1 eq) of Ru20 in 10 mL THF and 13.2 mg (0.055 mmol, 1.1) of L4b was added to the solution. A color change from green to red was observed immediately. After 30 min the reaction was completed, and the solvent was removed under reduced pressure. The crude reaction mixture was redissolved in toluene, filtered through Celite and concentrated to about 2 mL. To this solution 10 mL hexane was added and cooled to -20 ºC for 15 h. The resulting solid was collected and washed with cold hexane (2 x 4 mL) to yield the desired product as red microcrystalline solid.

Yield: 16.0 mg (42 %).

^{1}H NMR (500 MHz, C6D6) δ 15.89 (s, 1H), 9.07 (d, J = 5.6 Hz, 1H), 8.06 (dd, J = 7.2, 0.9 Hz, 1H), 7.79 (dd, J = 7.6, 1.0 Hz, 1H), 7.55 – 7.49 (m, 1H), 7.12 (s, 1H), 7.10 – 7.05 (m, 1H), 6.95 (dt, J = 4.9, 1.0 Hz, 1H), 6.64 (tt, J = 7.5, 1.5 Hz, 2H), 6.57 (d, J = 0.9 Hz, 1H), 6.36 (dd, J = 3.8, 1.2 Hz, 1H), 6.30 (tt, J = 5.6, 1.5 Hz, 1H), 6.23 (t, J = 4.4 Hz, 1H), 6.21 (s, 2H), 5.88 (ddd, J = 6.9, 5.2, 1.4 Hz, 1H), 2.51 (s, 6H), 1.98 (s, 6H), 1.65 (br, 6 H) 1.36 (s, 6H), 0.94 (d, J = 0.9 Hz, 3H).

^{13}C-NMR (C6D6, 850 MHz): 261.0, 181.8, 165.3, 152.5, 151.6, 149.2, 144.3, 138.1, 134.6, 133.9, 132.3, 129.2, 129.0, 126.1, 123.3, 122.9, 119.2, 116.9, 113.6, 101.7, 20.7, 18.5, 14.4, 8.8.

HRMS(ESI+) m/z: [M-NC5H5]+ Calcd for C37H39N3RuS2 690.1550; Found 690.9360.

Elemental Analysis: Anal. Calcd for C42H44N4RuS2 · 0.1 CH2Cl2: C, 64.95; H, 5.72; N,7.20. Found: C, 64.60; H, 5.53; N, 6.74. The 0.1 eq DCM were determined from a 1H NMR spectrum of the sample in C6D6. Due to the lability of the bound pyridine, prolonged time under reduced pressure, led to partial decomposition of the catalyst.

Synthesis of Complex Ru21c

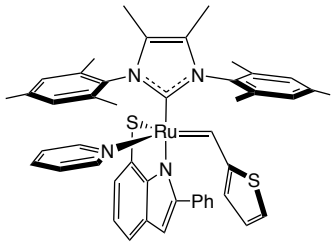

In a glovebox, a 20 mL vial was charged with 60.0 mg (0.08 mmol, 1 eq) of **Ru20** in 10 mL THF and 27.3 mg (0.09 mmol, 1.1 eq) of **L4c** was added to the solution. A color change from green to red was observed immediately. After 30 min the reaction was completed, and the solvent was removed under reduced pressure. The crude reaction mixture was redissolved in toluene, filtered through a pad of Celite and concentrated to about 2 mL. To this solution 10 mL hexane was added and cooled to -20 ºC for 15 h. The resulting solid was collected and was washed with cold pentane (2 x 4 mL) to yield the desired product as red crystals.

Yield: 31.1 mg (46 %).

^{1}H NMR (850 MHz, C_6D_6) δ 15.87 (s, 1H), 8.86 (d, *J* = 5.4 Hz, 1H), 8.07 (dt, *J* = 7.3, 0.8 Hz, 1H), 7.74 (dt, *J* = 7.7, 0.7 Hz, 1H), 7.54 – 7.50 (m, 1H), 7.05 – 6.97 (m, 2H), 6.85 – 6.77 (m, 4H), 6.62 (td, *J* = 7.3, 1.0 Hz, 2H), 6.60 – 6.55 (m, 2H), 6.47 (tt, *J* = 7.4, 1.5 Hz, 1H), 6.18 (s, 6H), 5.78 (s, 2H), 2.56 – 1.84 (m, 18H), 1.32 (s, 6H).

^{13}C-NMR (C_6D_6, 850 MHz): 261.6, 181.2, 152.4, 152.3, 149.1, 148.1, 141.2, 140.4, 138.2, 133.8, 129.0, 126.5, 126.2, 123.6, 122.9, 122.4, 119.7, 117.6, 114.1, 104.9, 20.5, 18.4, 13.9, 8.7.

HRMS(ESI$^+$) m/z: $[M\text{-}NC_5H_5]^+$ Calcd for $C_{42}H_{41}N_3RuS_2$ 753.1785; Found 753.9206.

Elemental Analysis: Anal. Calcd for $C_{47}H_{46}N_4RuS_2 \cdot 0.1\ C_5H_{12}$: C, 69.07; H, 6.47; N,6.20. Found: C, 68.85; H, 4.63; N, 5.92. The 0.1 eq pentane were determined from a ^{1}H NMR spectrum of the sample in C_6D_6. Due to the lability of the bound pyridine, prolonged time under reduced pressure, led to partial decomposition of the catalyst.

Isomer Ru21a and Ru21a'

The ^{1}H NMR of the complex **Ru21a** shows a minor component **Ru21a'** (5%) with an alkylidene resonance at δ = 15.38 ppm. Several crystallization attempts, in toluene/pentane or DCM/pentane, did not change the **Ru21a**/**Ru21a'** ratio (19:1). This ratio is also temperature-independent in the range 10 – 50 °C, persistent in solution even with visible precipitation (decomposition) in a monitored J-Young tube (7 days), and constant during reaction with propene. Furthermore, a NOESY experiment of a solution containing **Ru21a** and **Ru21a'** (Fig. S1) shows a positive cross-signal between the alkylidene resonances of **Ru21a** and **Ru21a'**, confirming that the two isomers are in a dynamic equilibrium with each other. The free energy difference between the two isomers can thus be estimated as $\Delta G_{(\mathbf{Ru21a'-Ru21a})} = = 1.8$ kcal mol^{-1} (Eq. 1). Hoveyda and co-workers has previously shown that a bidentate dithiolate ligand can rotate to interchange the position of the two S atoms [5]. This suggests that the observed complex **Ru21a'** could be the less stable S,N rotamer of **Ru21a**. Indeed, the isomer with the S-atom located trans to the NHC ligand has a DFT-calculated free energy (relative to that of **Ru21a**) only 0.1 kcal/mol higher than that of the NOESY-derived energy difference ($\Delta G^{DFT}_{\mathbf{Ru21a}}$ = 1.9 kcal mol^{-1}, see the Computational Results section below), and we thus assume the observed minor component **Ru21a'** is due to this isomer.

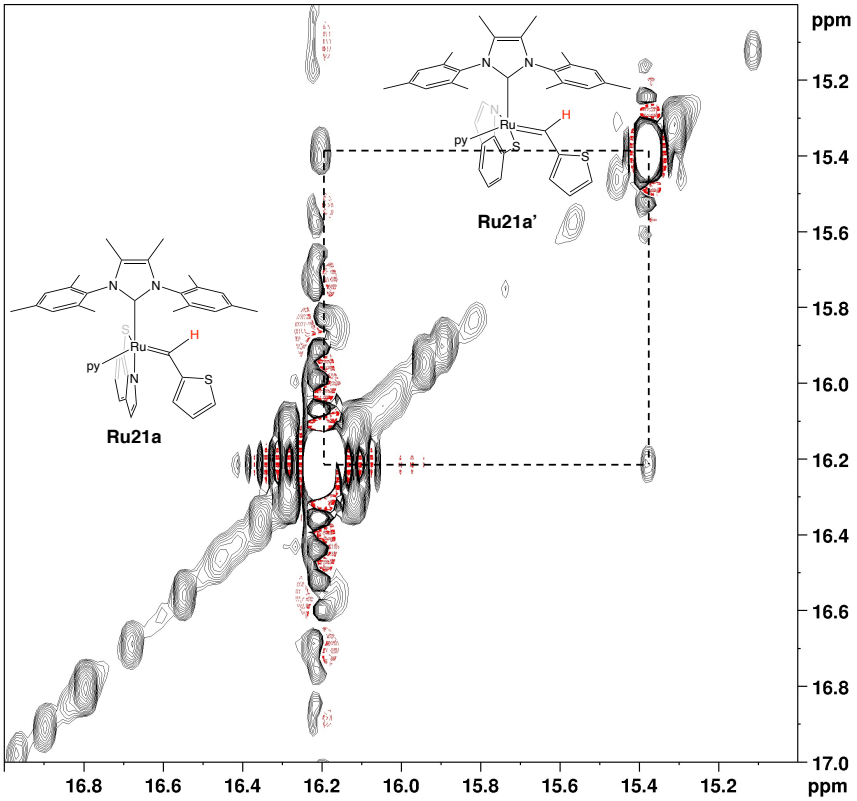

Fig. S1 NOESY-Experiment of complex **Ru21a** and Ru21a' showing the exchange between Ru21a and Ru21a' (C_6D_6, 850 MHz) (py = pyridine)

$$\Delta G_{(\mathrm{Ru21a'-Ru21a})} = -RT \ln K_{eq} = -RT \ln \frac{5}{95} = 1.8 \text{ kcal mol}^{-1} \qquad \text{(Eq. 1)}$$

Metathesis Reaction of catalysts Ru21a-b

Self-Metathesis of Styrene

In a 4 mL vial, a stock solution of catalyst Ru21a (19.6 mg, 0.026 mmol)) and anthracene (I.S., 4.6 mg, 0.026 mmol, 1 eq) in 2.6 mL C_6D_6 (10 mM in Ru) was made. The resulting solution was filtered through a pipette filter stuffed with a Kimwipe to remove any undissolved solids. 600 µL of this solution was transferred to a J-Young NMR tube. An initial ^{1}H NMR spectrum was recorded to establish a starting ratio between starting alkylidene vs anthracene. The J-Young NMR was reimported into the Glovebox and styrene (3.7 µL, 0.0325 mol, 5 eq) was added and the timer started. The solution was mixed in the NMR tube at 298 K, and ^{1}H NMR spectra were recorded periodically to track the disappearance of starting material and appearance of products over time. The experiment was repeated using a stock solution of Ru21b (15.4 mg, 0.026 mmol) with anthracene (I.S., 4.6 mg, 0.026 mmol, 1 eq) in 2.6 mL C_6D_6 (10 mM in Ru).

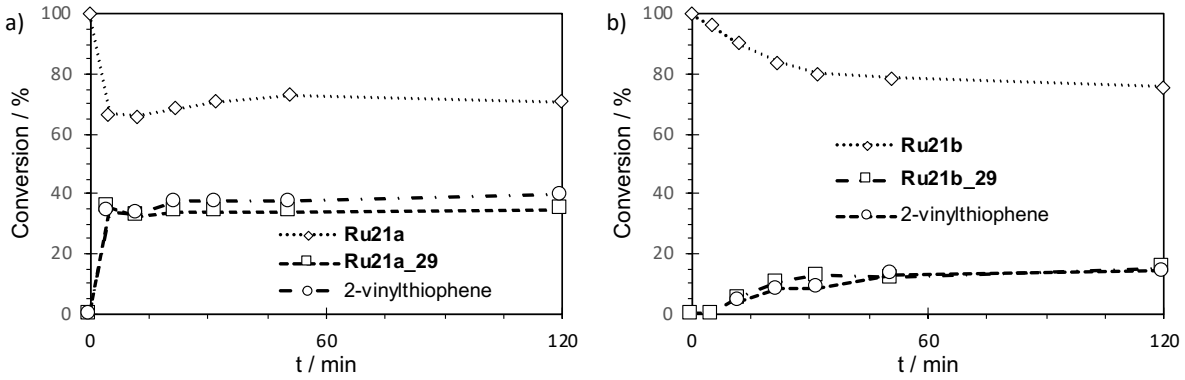

Fig. S2 Self-metathesis of styrene with catalyst **Ru21a** (a) and **Ru21b** (b) in C_6D_6 over 2 hours. No stilbene formation was observed, but new alkylidene signals emerged. The reaction was monitored by ^{1}H-NMR analysis relative to internal standard (See Fig. S3 and S4)

The reaction with styrene of both catalysts, **Ru21a** and **Ru21b**, showed no formation of stilbene (See Fig. S2 and S3). However, during the reaction a new alkylidene signal appeared at 17.2 ppm and 16.9 ppm, respectively, which correlates with the disappearance of the starting material (δ = 16.2 and 15.9 ppm,) and the formation of 2-vinylthiophene (C_5H_3S-C*H*$_2$: δ = 5.48, 4.89 ppm) [6]. The appearance of 2-vinylthiophene requires the exchange of the alkylidene with styrene via a non-productive metathesis (see Scheme S1). Therefore, the alkylidene signal was assigned to complex **Ru21a_29** and **Ru21b_29**. Interestingly, the equilibrium between **Ru21a** and **Ru21a_29** is reached immediately, while the equilibrium with the more sterically hindered complex **Ru21b** is reached after 30 min. The slower exchange indicates a higher energy barrier for olefin metathesis which agrees with the computational results (see Table S5).

Scheme S1 Alkylidene Exchange of Catalyst Ru21a and Ru21b with Styrene via Non-Productive Metathesis

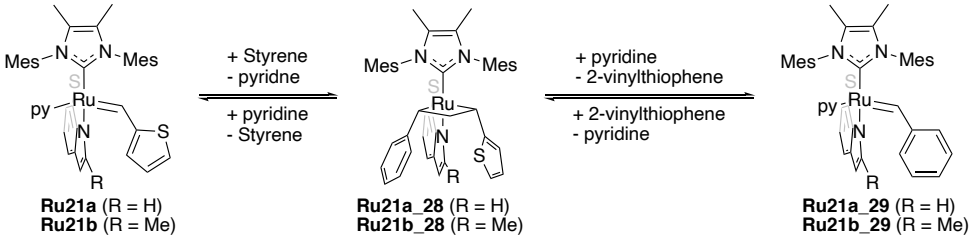

Ru21a (R = H)
Ru21b (R = Me)

Ru21a_28 (R = H)
Ru21b_28 (R = Me)

Ru21a_29 (R = H)
Ru21b_29 (R = Me)

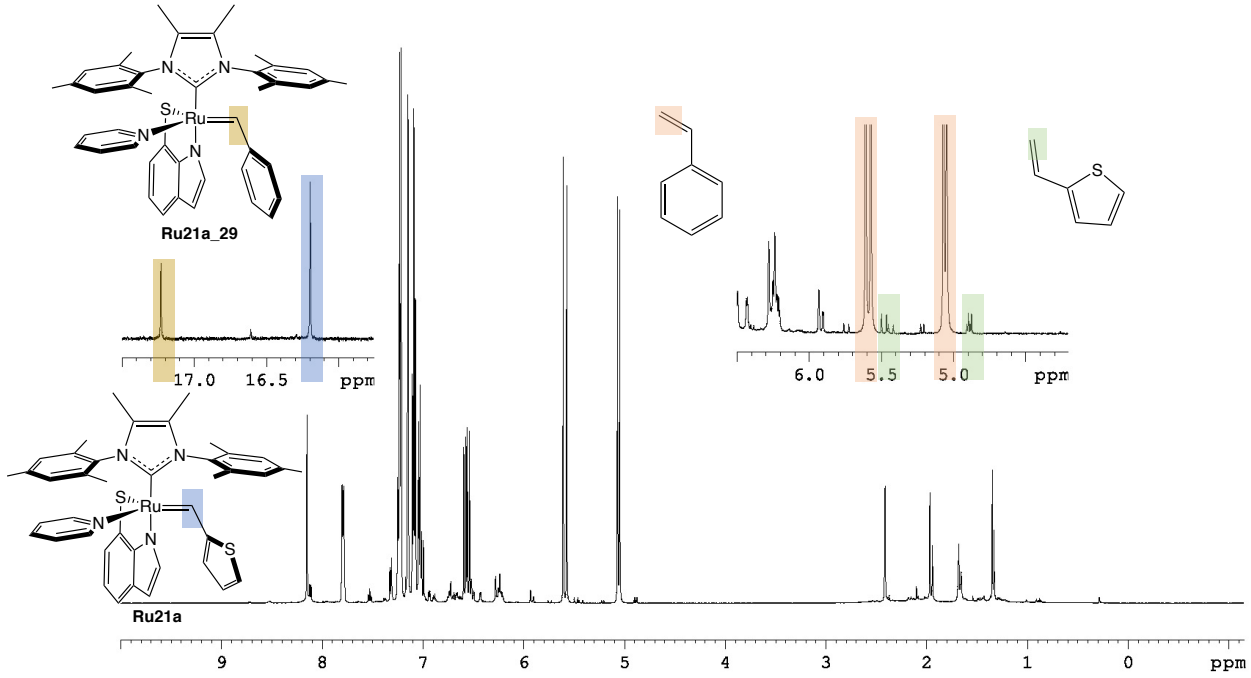

Fig. S3 ^{1}H NMR spectrum of reaction of catalyst **Ru21a** with 5 eq. styrene after 2 h. Inset shows the key organic products. The signals of 2-vinylthiophene are in agreement with literature [6]. (C_6D_6, 300.1 MHz)

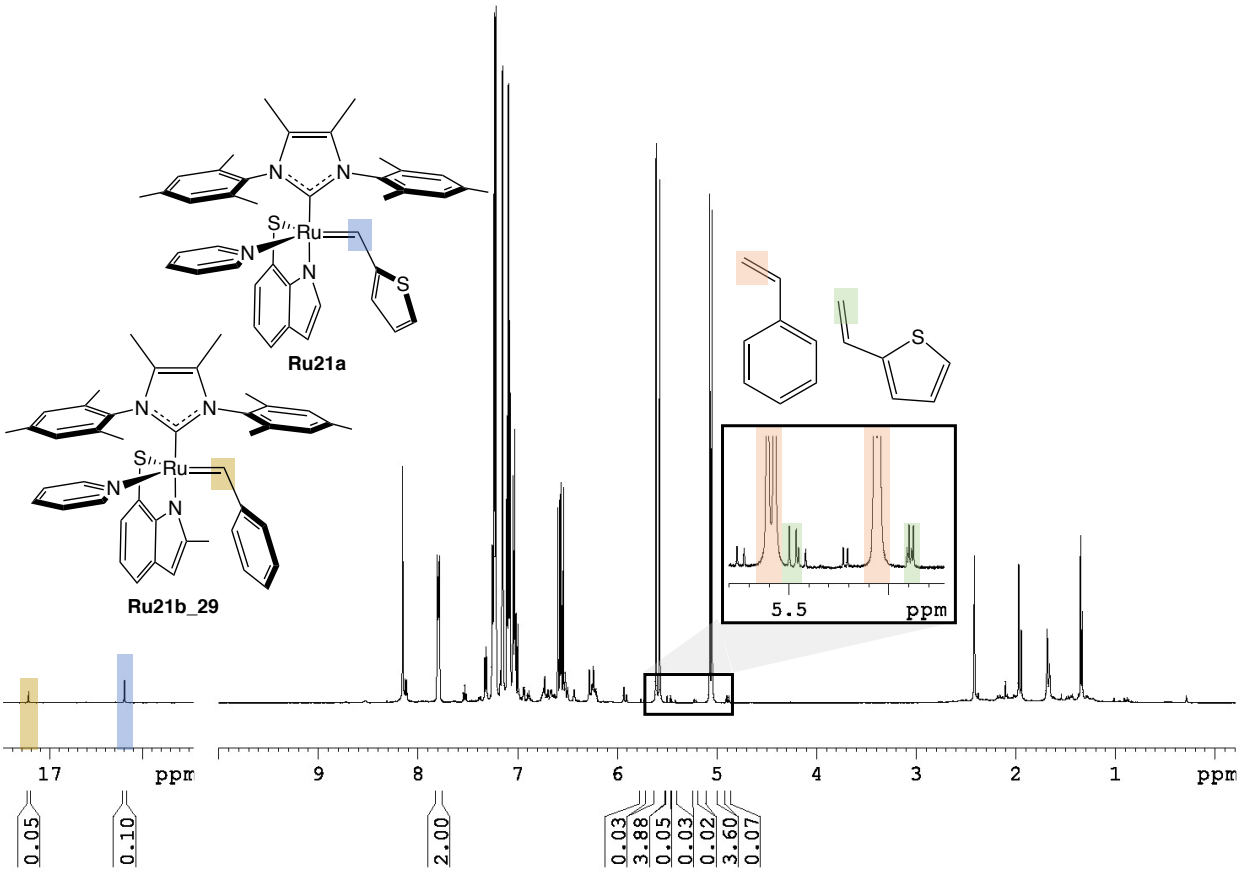

Fig. S4 ^{1}H NMR spectrum of reaction of catalyst **Ru21b** with 5 eq styrene after 2h. Inset shows the key organic products. The 2-vinylthiophene signals are in agreement with literature [6]. (C_6D_6, 300.1 MHz)

Self-Metathesis of Allylbenzene

(a) The stock solutions of the catalyst from the styrene experiment were used. Similarly, 600 µL of the solution containing **Ru21b** and anthracene was transferred to a J-Young NMR tube. An initial ^{1}H NMR spectrum was recorded to establish a starting ratio between starting alkylidene vs anthracene. The J-Young NMR was reimported into the Glovebox and allylbenzene (4.3 µL, 0.325 mmol, 5 eq) was added and the timer started. The solution was mixed in the NMR tube at 298 K and ^{1}H NMR spectra were recorded periodically to track the disappearing of starting material and appearing of products over time.

(b) In a 4 mL vial, a solution containing dodecane (I.S., 24.0 µL, 0.1 mmol) and allylbenzene (14.0 µL, 0.1 mmol) and 2 mL THF was made. An aliquot was taken to record the initial concentration. 1 mL of the THF solution was then added to a 4 mL vial containing catalyst **Ru21a** (2 mg, 0.0026 mmol, 5mol%) and the timer started. The reaction was conducted at room temperature. Aliquots were taken periodically and the reaction in each aliquot was quenched with ca. 10 equiv of potassium tris(pyrazolyl)borohydride. The samples were analyzed by GC/FID.

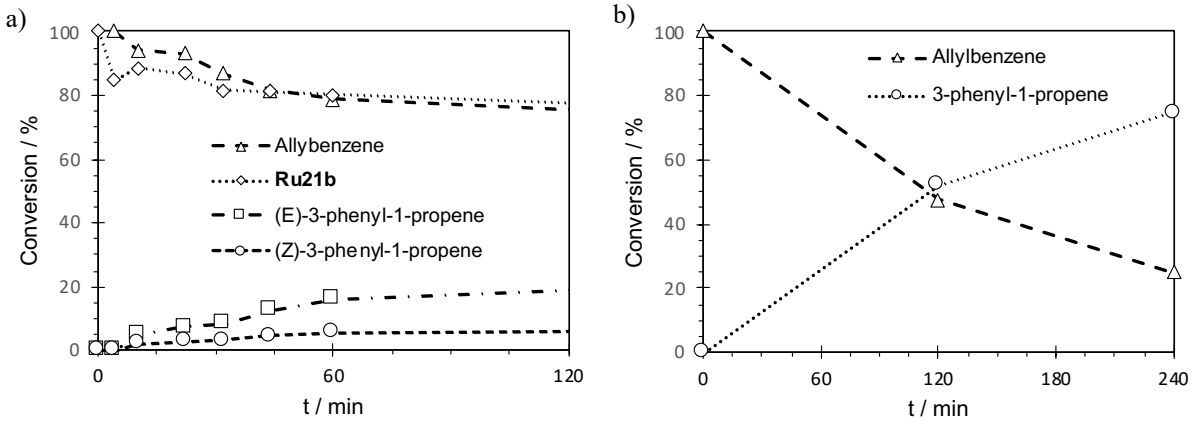

Fig. S5 Self-metathesis of allylbenzene with catalyst (a) **Ru21b** in C_6D_6 and (b) **Ru21a** in THF. Only isomerization allylbenzene to 3-phenyl-1-propene was observed. Reaction was monitored (a) by ^{1}H-NMR analysis relative to internal standard and (b) via GC analysis of aliquots

The reaction of catalyst **Ru21b** with allylbenzene showed no formation of 1,4-diphenylbut-2-ene. The isomerization of allylbenzene to 3-phenyl-1-propene (*E*:*Z,* 75:25) correlates with the disappearance of allylbenzene (Fig. S3). Since no metathesis occurred after 60 min, the J-Young NMR tube was heated to 50 °C for 12 h. After 12 h, still 17 % of catalyst **Ru21b** was visible, probably due to reduced initiation because of steric hindrance compared of catalyst **Ru21a**. Furthermore, after 12 h 2-vinylthiophene (C_5H_3S-C*H*$_2$: δ = 5.48, 4.89 ppm) [6] and styrene (C_7H_6-C*H*$_2$: δ = 5.60, 5.07 ppm) was observed. 2-Vinylthiophene is evidence for the occurrence of non-productive metathesis with allylbenzene. The formation of styrene is a product of metathesis with prop-1-en-1-ylbenzene forming a benzylidene complex. Styrene is then released by non-productive metathesis with allylbenzene.

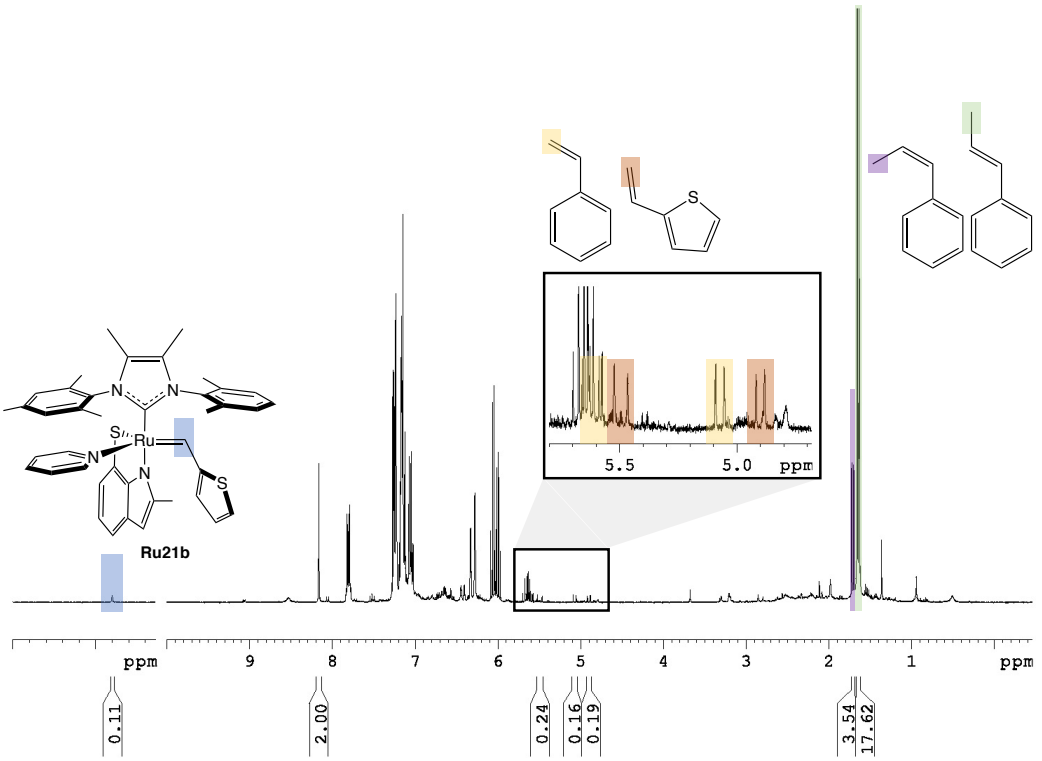

Fig. S6 ^{1}H NMR spectrum of reaction after 12 h at 50 °C of catalyst **Ru21b** with allylbenzene. Inset shows the key organic products. The signals of 3-phenylprop-2-ene, 2-vinylthiophene and styrene are in agreement with literature. (C_6D_6, 300.1 MHz)

Similarly, no 1,4-diphenylbut-2-ene was detected when a reaction of the smaller **Ru21a** with allylbenzene was followed via GC. Computational models indicate a higher barrier of the key intermediate, the rupture of the metallacyclobutane for catalyst **Ru21a**, for the formation of stilbene ($\Delta G^{\ddagger}_{TS29}$ = 36.9 kcal mol^{-1}, see Scheme S12) and 1,4-diphenylbut-2-ene ($\Delta G^{\ddagger}_{TS31}$ = 37.5 kcal mol^{-1}, see Scheme S12) reaching the kinetic limit for metathesis. The high barrier for the productive metathesis is caused by the steric congestion of metallacyclobutane (MCB) intermediate and of the corresponding cycloreversion transition state, which can be relieved via distortion of the metallacyclobutane geometry which also enables the decomposition of the catalyst via β-H elimination [7].

Self-Metathesis of Ethylene

In a 4 mL vial, catalyst **Ru21a** (14.3 mg, 0.02 mmol) and anthracene (I.S., 3.6 mg, 0.02 mmol, 1 eq) were dissolved in 1 mL C_6D_6 (20 mM Ru). The resulting solution was filtered through a pipette filter stuffed with a Kimwipe to remove any undissolved solids. 600 µL of this solution was transferred to a J-Young NMR tube. An initial ^{1}H NMR spectrum was recorded to establish a starting ratio between starting alkylidene vs anthracene. The NMR tube was attached to a Schlenk line and degassed (4 freeze-pump-thaw cycles), then allowed to thaw under ethylene atmosphere. After 3 min, the tube was sealed, shaken, and the timer started. A ^{1}H NMR spectrum was immediately recorded to confirm the presence of ethylene (δ = 5.25 ppm). Additional spectra were recorded periodically to track the disappearing of starting material and appearing of products over time at room temperature, see Fig. S8. For conversion plot, see Fig. S7. The ^{1}H NMR spectrum after 60 min showing [Ru]=CHR and organic products, see Fig. S8.

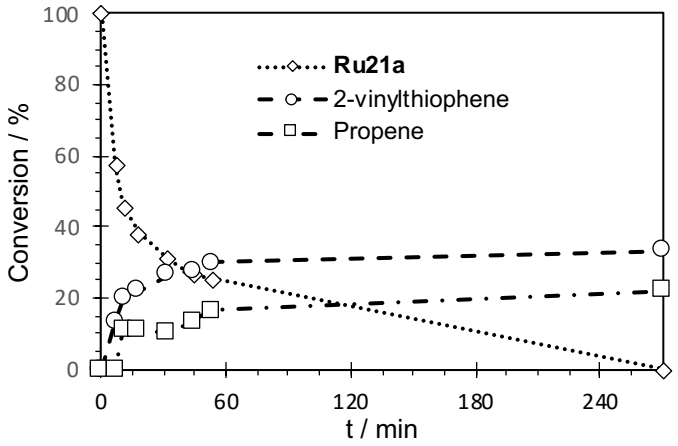

Fig. S7 Loss of precatalyst **Ru21a** with the formation of vinylthiopene and propene during the reaction with ethylidene in C_6D_6 (see Fig. S8 and S9). Reaction was monitored by ^{1}H-NMR analysis relative to internal standard

During the reaction with ethylene, the liberation of vinylthiophene (C_5H_3S-C*H*$_2$: δ = 5.48, 4.89 ppm) [6] indicates the initiation of the catalyst via non-productive metathesis. The propene (H_3CC*H*C*H*$_2$: δ = 5.71, 5.03, 4.97 ppm) is a decomposition product of the unsubstituted MCB (see Fig. S8). The reduced amount of propene compared to vinylthiophene is due to the gas phase-solvation equilibrium within the J-Young NMR tube. The catalyst **Ru21a** is completely decomposed after 270 min. The relative fast decomposition of catalyst **Ru21a** in ethylene compared to the reaction with allylbenzene is another indicator that the reaction with allylbenzene is hindered by steric reasons. Computational analysis of the reaction indicates that decomposition via β-hydride elimination (formation of propene) and nucleophilic attack are energetically similar (ΔΔG‡ = 0.2 kcal mol^{-1}, **Ru21a_TS22,24** vs **Ru21a_TS21,23**), see Scheme S8. and Table S7. Decomposition via nucleophilic attack would not release propene, thus explaining the low yield of it.

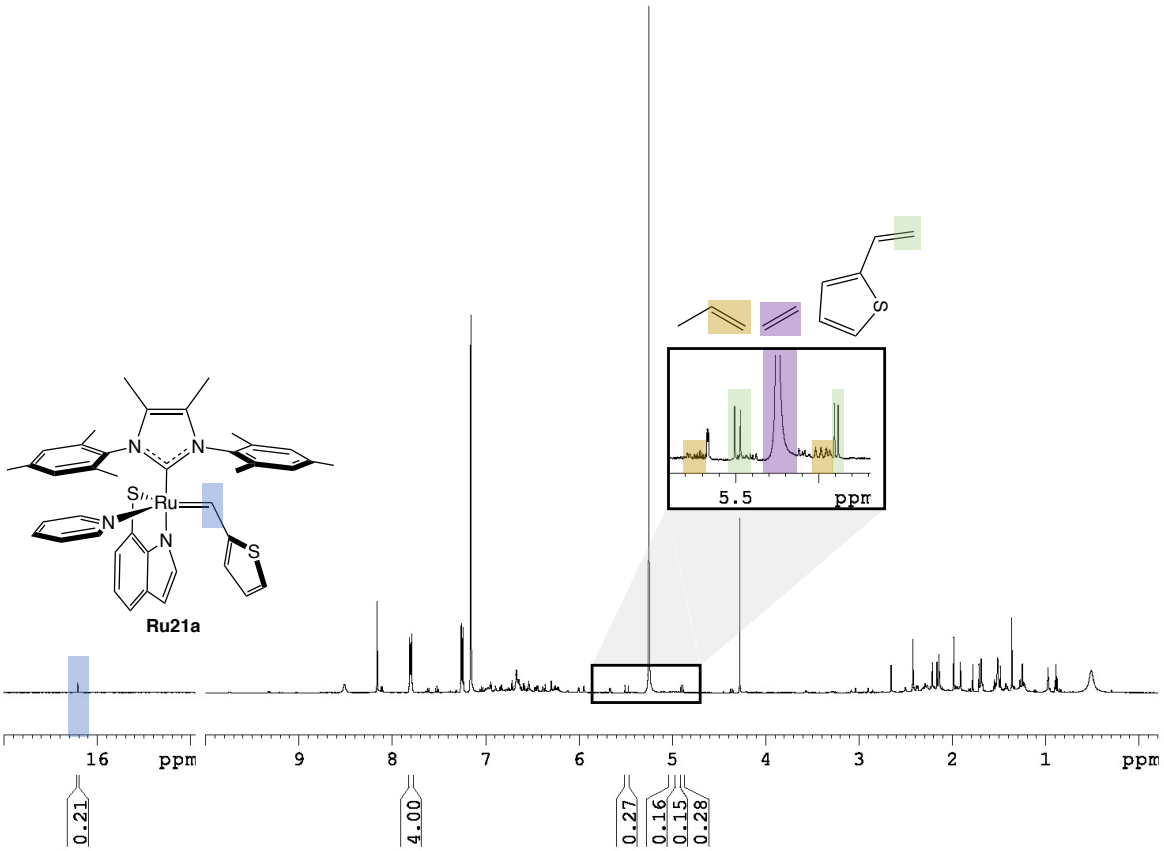

Fig. S8 ^{1}H NMR spectrum of reaction of catalyst Ru21a with ethylene, after 60 min. Inset shows the key organic products. The signals of 2-vinylthiophene and propene are in agreement with literature [6]. (C_6D_6, 300.1 MHz)

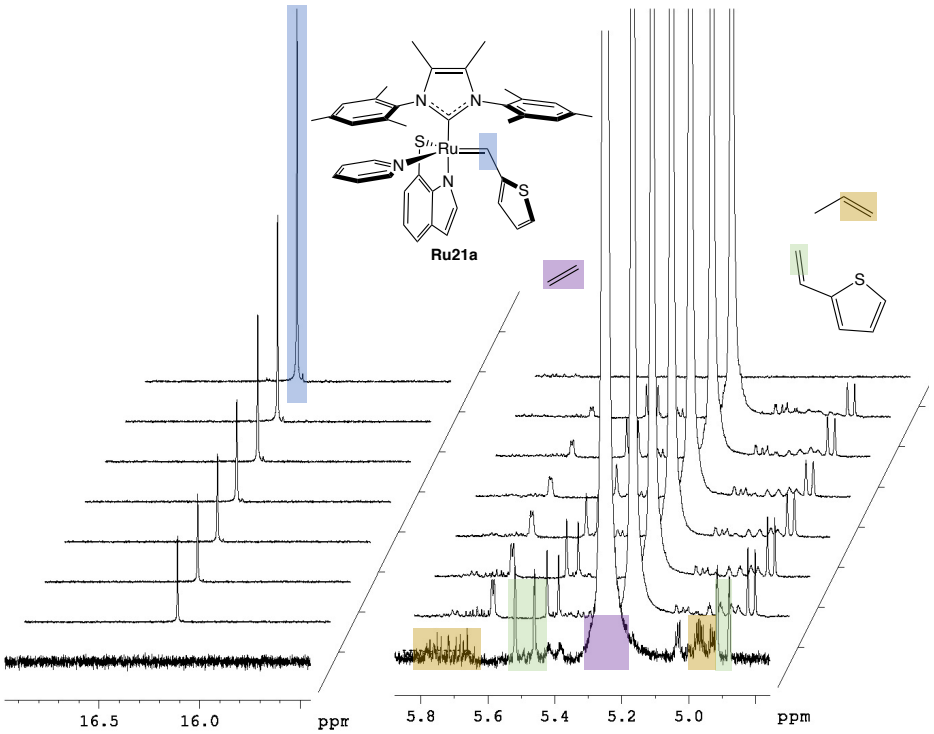

Fig. S9 Stacked ^{1}H NMR spectrum of reaction of catalyst **Ru21a** with ethylene. The signals of 2-vinylthiophene and propene are in agreement with literature [6]. (C_6D_6, 300.1 MHz)

Self-Metathesis of Propene

In a 4 mL vial, catalyst **Ru21a** (7.5 mg, 0.01 mmol) and hexamethylbenzene (I.S., 1.6 mg, 0.01 mmol, 1 eq) were dissolved in 1 mL C_6D_6 (20 mM Ru). The resulting solution was filtered through a pipette filter stuffed with a Kimwipe to remove any undissolved solids. 600 µL of this solution was transferred to a J-Young NMR tube. An initial ^{1}H NMR spectrum was recorded to establish a starting ratio between starting alkylidene vs hexamethylbenzene. The NMR tube was attached to a Schlenk line and degassed (4 freeze-pump-thaw cycles), then pressured with propene. The tube was sealed, shaken, and the timer started. A ^{1}H NMR spectrum was immediately recorded to confirm the presence of propene (δ = 5.72, 4.97 and 1.54 ppm). Additional spectra were recorded periodically to track the disappearing of starting material and appearing of products (ethylene (δ = 5.25 ppm), E-butene (δ = 5.38 ppm) and Z-butene (δ = 5.48 ppm)) over time. The selectivity was determined by the formation of *E*- and *Z*-butene in a quantitative ^{1}H-NMR experiment [8]. The experiment was repeated using **Ru21b** (7.6 mg, 0.01 mmol) and **Ru21c** (8.2 mg, 0.01 mmol), see Table S1.

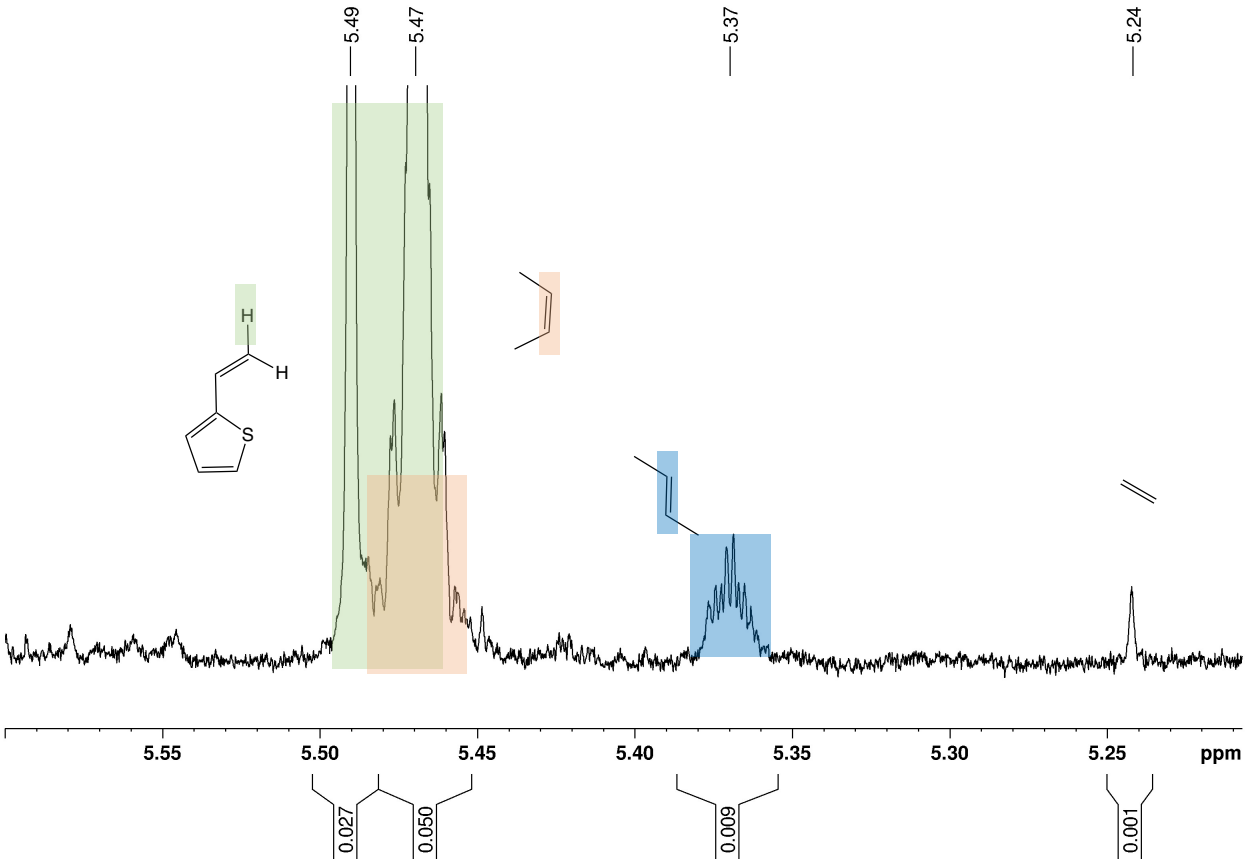

Fig. S10 ^{1}H NMR spectrum of reaction of catalyst **Ru21a** with propene. The signals of vinylthiophene, Z-Butene, E-Butene and ethylene are in agreement with literature **[6,9]**. Due to overlapping of 2-vinylpropene and Z-butene, Z-Butene (orange) was determined by the different between the two signals of the doublet of 2-vinylpropene (green) (C_6D_6, 850 MHz)

Table S1 The Stereoselectivity of Propene Metathesis Using Ru13 and Ru21a. No Butene Was Obtained using Ru21b and Ru21c

Entry	Catalyst	Selectivity[a] E:Z	$\Delta\Delta G^{\ddagger}_{(E/Z)}$-[b] [kcal mol^{1}]	TON[c]
1	**Ru13**	17:83	-0.9	-
2	**Ru21a**	23:77	- 0.7	-
3	**Ru21b**	-		-
4	**Ru21c**	-		-

a Selectivity was determined by the ratio of E-butene and Z-butene in solution, see Fig. S10. b Derived from the observed stereoselectivity via the Eyring equation. c Due to the low conversion, turnover numbers were not determined.

S3. Computational Methods

DFT calculations were performed with Gaussian 16 with revisions C.01 [10] using the built-in ultrafine grid for numerical integrations.

Geometry Optimization

Three different density functionals were considered for geometry optimization; see the below subsection on validation of the various computational approaches. The functionals considered for geometry optimization were: PBE [11] (Approach A), ωB97XD [12] (Approach B) and M06-L [13-15] (Approach C). All PBE calculations included Grimme's empirical D3 dispersion corrections [16], with revised Becke–Johnson damping parameters (labelled D3(MBJ) for brevity) [17]. The Stuttgart/Cologne 28-electron relativistic effective core potentials (ECP28MDF) [18] were used for Ru atoms, in conjunction with the corresponding correlation-consistent valence double-ζ plus polarization basis set augmented by diffuse functions (aug-cc-pVDZ-PP) [18], as obtained from the Stuttgart/Cologne basis set repository[1]. Correlation-consistent, valence double-ζ plus polarization basis sets (cc-pVDZ [19] from the EMSL basis set exchange website) [20] were used for H, C, H and O atoms, whereas a corresponding quadruple-ζ plus polarization basis set (cc-pVQZ) [19] was used for S atoms.

Geometries were optimized using tight convergence criteria (max. force $1.5 \cdot 10^{-5}$ a.u., RMS force $1.0 \cdot 10^{-5}$ a.u., max. displacement $6.0 \cdot 10^{-5}$ a.u., RMS displacement $4.0 \cdot 10^{-5}$ a.u.), without symmetry constraints, using tighter convergence criteria for the self-consistent field (SCF) optimization procedure (RMS change in density matrix $< 1.0 \cdot 10^{-9}$, max. change in density matrix $=1.0 \cdot 10^{-7}$), and with a spin multiplicity of 1. All stationary points were confirmed to be either minima (all-positive Hessian eigenvalues) or transition states (a single negative Hessian eigenvalue) by analytical calculation of the second derivatives, i.e., the Hessian matrix. Textbook procedures were used to calculate the translational, rotational, and vibrational components of the thermal corrections to enthalpies and Gibbs free energies within the ideal-gas, rigid-rotor, and harmonic oscillator approximations, with one exception: All frequencies below 100 cm^{-1} were shifted to 100 cm^{-1} when calculating the vibrational component of the entropy, which is often referred to as the quasi-harmonic oscillator approximation [15,21]. This approach is aimed at preventing breakdown (i.e., the asymptote corresponding to infinite entropy) of the harmonic approximation for low-frequency modes [22].

Single-Point Energy Calculations

The geometries obtained as described above were adopted in single-point energy calculations using the PBE [11] and M06-L [13-15] functionals in conjunction with the PCM [23] polarizable continuum solvent model, with default parameters for benzene as solvent. All PBE calculations included Grimme's empirical D3 dispersion corrections [16], with revised Becke–Johnson damping parameters (labelled D3(MBJ) for brevity) [17]. In all single-point calculations, the above basis set were extended to the valence quadruple-ζ level. Specifically, Ru was described by combining the 28-electron relativistic effective core potential (ECP28MDF) [18] with the corresponding correlation-consistent valence quadruple-ζ plus polarization basis set augmented by

[1] Energy-consistent Pseudopotentials of the Stuttgart/Cologne Group (http://www.tc.uni-koeln.de/PP/clickpse.en.html)

diffuse functions (aug-cc-pVQZ-PP) [18] from the Stuttgart/Cologne basis set repository [20]. The other atoms were described by correlation-consistent, valence quadruple-ζ plus polarization basis sets (cc-pVQZ [19] from the EMSL repository) [20]. The convergence criteria for the SCF procedure were relaxed in single-point calculations (RMS change in density matrix < 1.0·10−5, max. change in density matrix < 1.0·10−3).

Free Energies Calculations Including Standard State Correction

Free energies in solution were calculated from the following:

$G_X = E_X + \Delta G_{Y,qh}^{T=298.15\,K} + \Delta G_{1atm \to 1M}^{T=298.15\,K}$,

where $\boldsymbol{E_X}$ is the SP energy calculated with the computational model X, where X = PBE-D3(MBJ)-PCM(Benzene), or M06L-PCM(Benzene), $\Delta G_{Y,qh}^{T=298.15\,K}$, where Y = PBE- D3(MBJ), ωB97XD or M06L, is the thermal correction to the Gibbs free energy calculated at the geometry-optimization level with the quasi-harmonic oscillator approximation as described above, and $D\boldsymbol{G}_{1atm \to 1M}^{\boldsymbol{T=298.15\,K}}$ is the standard state correction from the ideal gas at 1 atm to a 1 M solution (but exhibiting infinite-dilution, ideal-gas-like behavior), which is equal to 1.89 kcal/mol at RT [24].

S4. Validation and Selection of the Computational Approach

Choice of Functional for Geometry Optimization

The design of an E-selective catalyst is delicate as the difference between the two rate-determining transition states between the E-and Z-pathway may be tiny. Therefore, three computational approaches, A, B, and C, were validated against the experimentally observed stereoselectivity of propene metathesis using the known catalyst **Ru13** (Table S2). The latter catalyst may be regarded as the parent of the thio-indolate catalysts designed in this work.

Approach A: Geometries were optimized using PBE- D3(MBJ)/cc-pVDZ. Single-point energy calculations were performed using PBE-D3(MBJ)/cc-pVQZ and M06-L/cc-pVQZ in conjunction with the PCM polarizable continuum solvent model to account for solvation effects using default parameters for benzene as solvent.

Approach B: Geometries were optimized using wB97XD/cc-pVDZ Single-point energy calculations were performed using PBE-D3(MBJ)/cc-pVQZ and M06-L/cc-pVQZ in conjunction with the PCM polarizable continuum solvent model to account for solvation effects using default parameters for benzene as solvent.

Approach C: Geometries were optimized using M06L/cc-pVDZ. Single-point energy calculations were performed using PBE-D3(MBJ)/cc-pVQZ and M06-L/cc-pVQZ in conjunction with the PCM polarizable continuum solvent model to account for solvation effects using default parameters for benzene as solvent.

Table S2: The Stereoselectivity of Propene Metathesis Using Catalyst Ru13 as Predicted by Computational Approaches A-C.

Approach	Model ID	$\boldsymbol{E}$ [a.u.]	$\Delta G_{qh}^{T=298.15\,K}$ [a.u.]	$E_{\mathrm{PBE-D3(MBJ)-PCM(benzene)}}$ [a.u.]	$E_{\mathrm{M06L-PCM(benzene)}}$ [a.u.]	$\Delta G_{\mathrm{PBE-D3(MBJ)-PCM(benzene)}}$ [kcal/mol]	$\Delta G_{\mathrm{M06L-PCM(benzene)}}$ [kcal/mol]
A	**Ru13_TS4,5$_E$**	-3161.106433	0.535016	-3161.083020	-3163.200665	0.0	0.0
	Ru13_TS4,5$_Z$	-3161.108143	0.535273	-3161.083373	-3163.202574	-0.2	-1.2
B	**Ru13_TS4,5$_E$**	-3162.956002	0.560327	-3161.060050	-3163.187954	0.0	0.0
	Ru13_TS4,5$_Z$	-3162.956957	0.559158	-3161.062104	-3163.189691	-1.3	-1.1
C	**Ru13_TS4,5$_E$**	-3163.265390	0.553430	-3161.066822	-3163.194177	0.0	0.0
	Ru13_TS4,5$_Z$	-3163.267741	0.553282	-3161.067650	-3163.196344	-0.5	-1.4

The suffix **TS4,5$_E$** indicates the rupture for the MCB forming E-Butene and **TS4,5$_Z$** for the formation of Z-Butene (see Scheme S2)

Expressed (via the Eyring equation) as a difference in free energy between the rate-determining transition states leading to (Z)- or (E)-2-butene, i.e., $\Delta\Delta G^{\ddagger}_{(E/Z)} = \Delta G^{\ddagger}_{Z} - \Delta G^{\ddagger}_{E}$, the experimentally determined stereoselectivity of propene metathesis using catalyst **Ru13** is $\Delta\Delta G^{\ddagger}_{(E/Z)}$ = -0.9 kcal mol^{-1}(see

Table S1). Using Approach B, PBE and M06L predict E-selectivities that are slightly too high but quite consistent. Therefore, ωB97XD was chosen as the standard functional for geometry optimization in this work.

Choice of Functional for Single-Point Calculations

Based on the experimentally observed stereoselectivity of catalyst **Ru13**, Approach B, i.e, the wB97XD functional, was chosen for geometry optimization. Among the two functionals tested for single-point energy calculations, PBE and M06L, only PBE predicts the correct orientation of the bidentate S,N-ligand in the catalyst precursor, i.e., M06L predicts Ru21a' to have lower energy than Ru21a (see Table S6). Moreover M06L also predicts, in contrast to experimental observation,[5] Ru18 to initiate faster than Ru13 (see Table S4). Therefore, PBE, in conjunction with empirical dispersion corrections to give the overall functional here labeled PBE-D3(MBJ), was chosen as the standard functional for single-point energy calculations in the present work.

S5. Computational Results

Calculated Barrier Heights and Kinetic Feasibility: Initial Considerations

Relying on transition-state theory, the relation between the rate constant k of a reaction and the corresponding activation free energy, $\Delta G^{\ddagger}$ is given by the Eyring equation as $k = \frac{k_B T}{h}\, e^{\frac{-\Delta G^{\ddagger}}{RT}}$ or, equivalently, as $\Delta G^{\ddagger} = -RT \ln\left(\frac{kh}{k_B T}\right)$. We may thus use the activation free energy as an indicator of the feasibility of a chemical reaction, i.e., whether it can be expected to occur within the time available. For example, for a unimolecular reaction ($A \rightarrow B$), the relation between the half-life $t_{1/2}$ and reaction rate k is $k = \frac{t_{1/2}}{\ln 2}$. The activation free energy corresponding to different half-lives is thus given by Equation 2.

$$\Delta G^{\ddagger} = -RT \ln\left(\frac{\ln(2)\, h}{k_B T t_{1/2}}\right) \qquad \text{(Eq. 2)}$$

Examples of pairs of half-lives and activation free energies that obey Equation 2 are given in Table S3.

Table S3 Examples of Pairs of Half-Lives $t_{1/2}$ and Activation Free Energies $\Delta G^{\ddagger}$ obeying Equation 2

Half life $t_{1/2}$	$\Delta G^{\ddagger}$ [kcal mol^{-1}]
2 h	22.9
1 d	24.4
7 d	25.5
31 d	26.4
365 d	27.9

with T = 298 K, R = 1-985 · 10^{-3} kcal K^{-1} mol^{-1}, h = 6.626 · 10^{-3}4 J S, k_B = 1.380 · 10-23 J K^{-1}

The estimates in Table S3 suggest that reactions start to become impractical at room temperature when the activation free energy rises above 25 kcal/mol. Allowing for some inaccuracies in DFT-calculated relative free energies, we may therefore expect reactions with DFT-estimated activation free energies above 30 kcal/mol to be unrealistic at room temperature [25].

Computational Results for Complexes Ru13, Ru18 and Ru19a-c.

Scheme S2 Energy Profile for the Productive Metathesis of Ru13 with Propene leading to (E)-2-Butene (full) and (Z)-2-Butene (dashed)

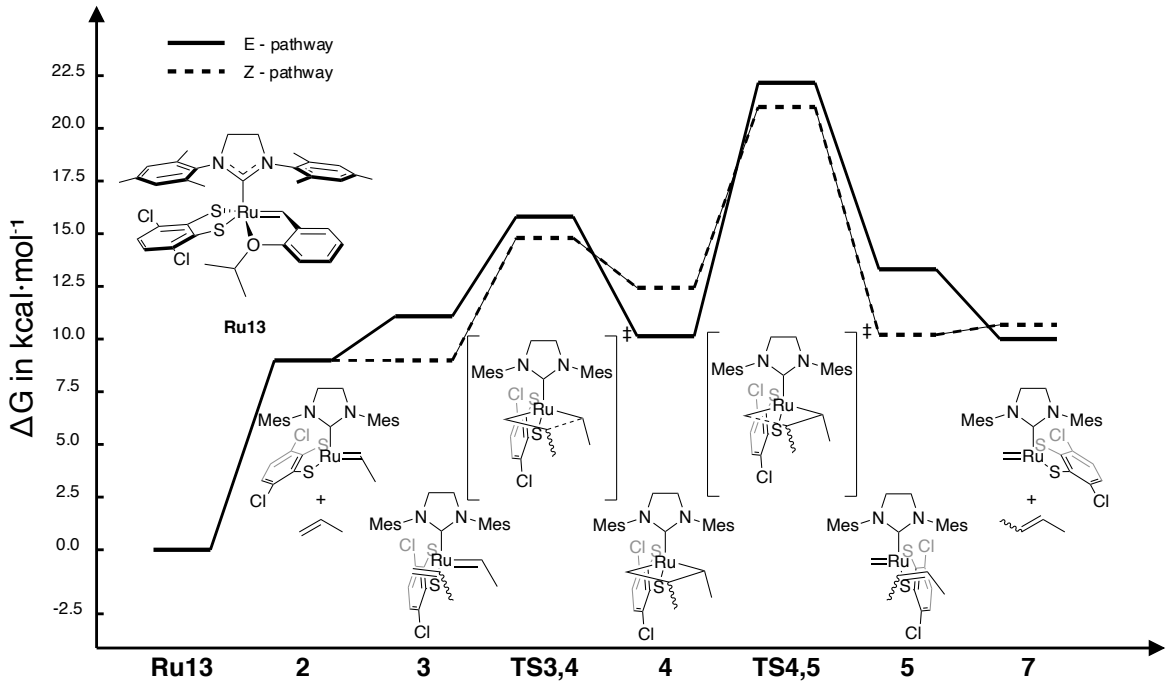

Scheme S3 During the Regeneration of the Active Species Ru13_2, the Catalyst is prone to decompose via nucleophilic attack Ru13_TS18,19

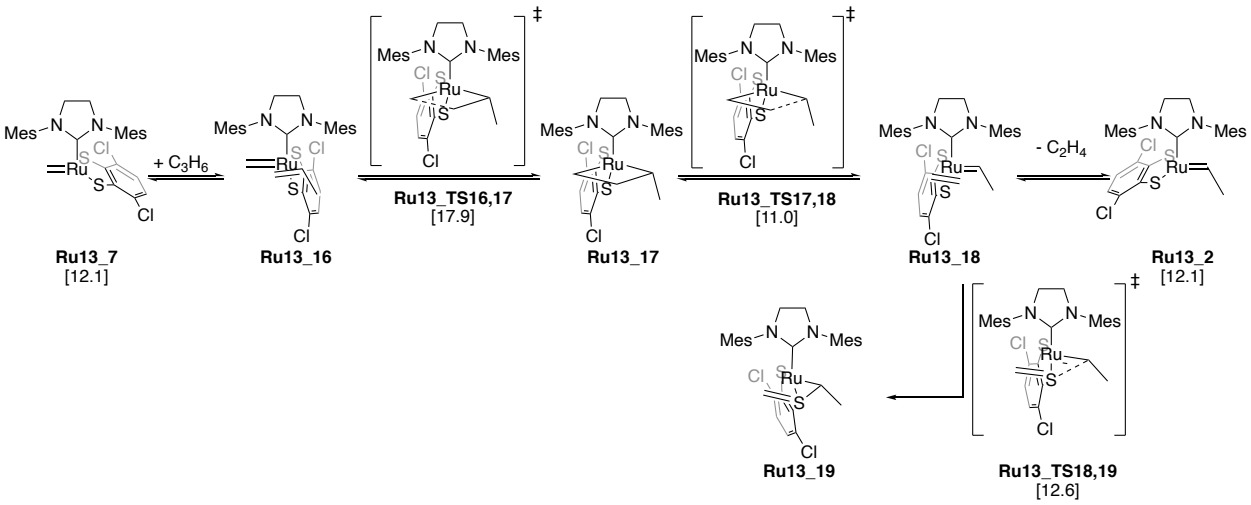

Chart S1 Additional Structure for Precursor Ru18 (a) and Ru13 (b-d), Showing the Unsubstituted MCB and Decomposition via c) β-Hydride Elimination and d) Nucleophilic Attack during Productive Metathesis

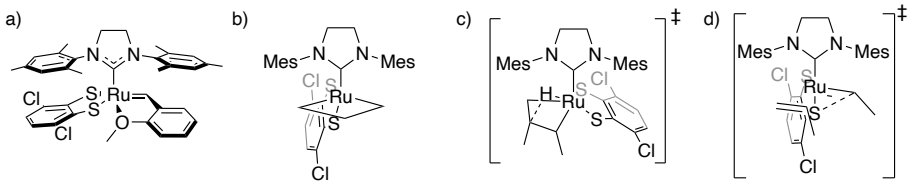

Ru18
[-0.5]

Ru13_22
[3.2]

Ru13_TS3,8$_Z$
[12.5]

Ru13_TS4,9$_Z$
[17.5]

Table S4 Gibbs Free Energies Calculated for Propene Metathesis Using Catalyst Ru13 Displayed in Scheme S2, Scheme S3 and Chart S1[a]

Model ID	$E_{\omega B97XD}$ [a.u.]	$\Delta G^{T=298.15\,K}_{\omega B97XD,qh}$ [a.u.]	$E_{PBE-D3M(BJ)-PCM(benzene)}$ [a.u.]	$E_{M06L-PCM(benzene)}$ [a.u.]	$\Delta G_{PBE-D3M(BJ)-PCM(benzene)}$ [kcal/mol][a]	$\Delta G_{M06L-PCM(benzene)}$ [a] [kcal/mol]
Ru13	-3429.915882	0.618805	-3428.443990	-3430.839043	0.0	0.0
Ru18	-3351.301249	0.562961	-3349.889345	-3352.190338	-0.5	4.4
Ru13_2	-3045.082345	0.477603	-3043.816001	-	9.0	-
Ru13_3$_E$	-3162.976186	0.564371	-3161.632534	-	11.1	-
Ru13_3$_Z$	-3162.974397	0.560697	-3161.632110	-	9.0	-
Ru13_TS3,4$_E$	-3162.967268	0.560938	-3161.621480	-	15.8	-
Ru13_TS3,4$_Z$	-3162.968273	0.560583	-3161.622805	-	14.8	-
Ru13_4$_E$	-3162.980512	0.560326	-3161.630040	-	10.1	-
Ru13_4$_Z$	-3162.979753	0.564127	-3161.630109	-	12.4	-
Ru13_TS4,5$_E$	-3162.956002	0.560327	-3161.610703	-	22.2	-
Ru13_TS4,5$_Z$	-3162.956957	0.559158	-3161.611420	-	21.0	-
Ru13_5$_E$	-3162.968283	0.561501	-3161.626063	-	13.3	-
Ru13_5$_Z$	-3162.973114	0.560132	-3161.629651	-	10.2	-
Ru13_7$_E$	-3005.766850	0.451525	-3004.528870	-	11.9	-
Ru13_7$_Z$	-3005.766850	0.451525	-3004.528870	-	12.6	-
Ru13_TS3,8$_Z$	-3162.963995	0.561112	-3161.619072	-	17.5	-
Ru13_TS4,9$_Z$	-3162.964283	0.561428	-3161.627230	-	12.5	-
Ru13_TS16,17	-3123.651078	0.533234	-3122.334439	-	17.9	-
Ru13_TS17,18	-3123.661517	0.532916	-3122.345132	-	11.0	-
Ru13_TS18,19	-3123.658421	0.532949	-3122.342640	-	12.6	-
Ru13_22	-3084.369671	0.509590	-3083.078212	-	3.2	-
Isopropoxystyrene	-502.669414	0.186608	-502.395132	-502.947572	-	-
Methoxystyrene	-424.051895	0.133273	-423.842229	-424.308368	-	-
Propene	-117.870108	0.054855	-117.790929	-117.939778	-	-
Ethylene	-78.560878	0.028971	-78.508999	-78.612024	-	-

a See Scheme S2, Scheme S3 and Chart S1for molecular structures.

Table S5 Gibbs Free Energies calculated for the Rate-Determining Transition State (Rupture of the Metallacyclobutane) of the *E*- and *Z*-pathway of Propene Metathesis of complex Ru19a-c

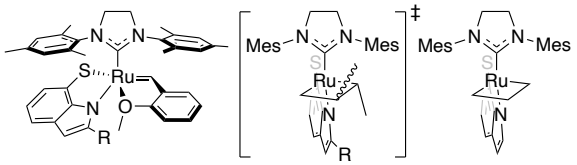

Ru19a R = H
Ru19b R = Me
Ru19c R = Ph

Ru19a_TS4,5 R = H
Ru19b_TS4,5 R = Me
Ru19c_TS4,5 R = Ph

Ru19a_22

Model ID	Substitutent R	$E_{\omega\mathrm{B97XD}}$ [a.u.]	$\Delta G_{\omega\mathrm{B97XD},qh}^{T=298.15\,K}$ [a.u.]	$E_{\mathrm{PBE-D3M(BJ)-PCM(benzene)}}$ [a.u.]	$E_{\mathrm{M06L-PCM(benzene)}}$ [a.u.]	$\Delta G_{\mathrm{PBE-D3M(BJ)-PCM(benzene)}}$ [kcal/mol]	$\Delta G_{\mathrm{M06L-PCM(benzene)}}$ [kcal/mol]
Ru19a	H	-2165.396001	0.613910	-2164.387625	-2166.315982	0.0	0.0
Ru19a_22	H	-1898.470826	0.558601	-1897.584819	-1899.257749	-0.9	-3.8
Ru19a_TS4,5$_E$	H	-1977.055101	0.610232	-1976.115625	-1977.881986	17.9	13.8
Ru19a_TS4,5$_Z$	H	-1977.049754	0.609467	-1976.109430	-1977.875135	21.3	17.7
Ru19b	Me	-2204.703290	0.640500	-2203.665344	-2205.641347	0.0	0.0
Ru19b_TS4,5$_E$	Me	-2016.359743	0.636485	-2015.391014	-2017.206420	19.1	14.2
Ru19b_TS4,5$_Z$	Me	-2016.354106	0.636110	-2015.384219	-2017.199423	23.2	18.4
Ru19c	Ph	-2396.402809	0.692316	-2395.262202	-2397.437938	0.0	0.0
Ru19c_TS4,5$_E$	Ph	-2208.052638	0.687222	-2206.978894	-2208.991215	24.1	20.9
Ru19c_TS4,5$_Z$	Ph	-2208.032632	0.686810	-2206.960226	-2208.973542	35.5	31.8

Computational Results for Complexes Ru21

The Catalyst Precursors Ru21a-c. A minor, constant alkylidene resonance ∂ = 15.38 ppm always occurred alongside the resonance of **Ru21a**, in a 5:95 ratio. The minor component could not be isolated, and its identification via experimental methods (NMR, MS, X-ray) was thus not possible. The structure of this component was, instead, inferred with the help of DFT calculations and NOESY experiment (Fig. S1). The NOESY experiment shows that the two alkylidene species are in equilibrium with each other in solution.

The most obvious candidate for this component (labeled **Ru21a'**) is that of an isomer with the S,N ligand rotated compared to **Ru21a**, i.e, an isomer with the thiolate sulfur atom trans, and the indolate nitrogen atom cis, to the NHC. Indeed, DFT predicts a $\Delta G_{Ru21a'/Ru21a}$ (1.9 kcal mol^{-1}, Table S6) almost identical to that of the NOESY experiments ($\Delta G^{Exp}_{7a'/7a}$ = 1.8 kcal mol^{-1}).

No corresponding minor component was observed in the ^{1}H NMR spectra of **Ru21b** and **Ru21c**, which is in agreement with the much lower DFT-predicted stability for the rotated S,N-ligands in these complexes ($\Delta G_{Ru21b'/Ru21b}$ = 4.0 kcal mol^{-1} and $\Delta G_{Ru21c'/Ru21c}$ = 11.3 kcal mol^{-1}). In both **Ru21b'** and **Ru21c'**, the larger substituent at position 2 of the indole ring experiences substantial steric repulsion against NHC mesityl-groups.

Table S6 Gibbs Free Energies of Catalysts Ru21a-c and their Isomers

Model ID	$E_{\omega B97XD}$ [a.u.]	$\Delta G^{T=298.15\,K}_{\omega B97XD,qh}$ [a.u.]	$E_{PBE-D3M(BJ)-PCM(benzene)}$ [a.u.]	$E_{M06L-PCM(benzene)}$ [a.u.]	$\Delta G_{PBE-D3M(BJ)-PCM(benzene)}$ [kcal/mol][a]	$\Delta G_{M06L-PCM(benzene)}$ [a] [kcal/mol]
Ru21a	-2697.355932	0.664475	-2696.109762	-2698.343345	0.0	0.0
Ru21a'	-2697.360618	0.666795	-2696.109034	-2698.346686	1.9	-0.6
Ru21b	-2736.665839	0.691396	-2735.390335	-2737.672841	0.0	0.0
Ru21b'	-2736.667085	0.692509	-2735.385095	-2737.674362	4.0	-0.3
Ru21c	-2928.362067	0.741391	-2926.983308	-2929.463517	0.0	0.0
Ru21c'	-2928.353369	0.744667	-2926.968584	-2929.453291	11.3	8.5

Catalytic Cycle and Decomposition Reactions. Low catalytic activity and low turnover numbers were obtained in metathesis experiments using one of the **Ru21** compounds (the mixture of isomers **Ru21a/Ru21a'**). Surprisingly, in contrast to the E-selectivity initially predicted for the thio-indolate-coordinated catalysts **Ru19a** and **Ru21a**, the **Ru21a/Ru21a'** mixture gave ca. 73% (Z)-2-butene in propene metathesis, which corresponds, via the Eyring equation, to a $\Delta\Delta G^{\ddagger}_{E/Z} = -0.7$ kcal mol^{-1}. To uncover possible explanations for the difference between the predicted and observed stereoselectivity, we have conducted additional DFT calculations.

One possibility is that the minor component **Ru21a'** of the **Ru21a/Ru21a'** mixture is responsible for the observed Z-selectivity. Propene metathesis using both these isomers was therefore studied in DFT calculations (Scheme S4), at the outset with the stereoselectivity estimated as the free energy difference between the transition states of cycloreversion, the elementary step typically found to be rate determining [26], to give (E)- and (Z)-2-butene, respectively.

This approach predicts **Ru21a** to be E-selective ($\Delta\Delta G^{\ddagger}_{TS4,5_Z - TS4,5_E}$ = 1.9 kcal mol^{-1}) and **Ru21a'** to be weakly Z-selective ($\Delta\Delta G^{\ddagger}_{TS4,5'_Z - TS4,5'_E}$ = – 0.5 kcal mol^{-1}). The selectivity predicted for **Ru21a'** is close to that experimentally observed for the **Ru21a/Ru21a'** mixture, suggesting that the metathesis performed by the mixture might be due to **Ru21a'** rather than to the intended isomer **Ru21a**.

Scheme S4 Energy Profile for the Productive Metathesis of Ru21a (black) and Ru21a' (blue) with Propene Leading to (E)-2-butene (full) and (Z)-2-butene (dashed)

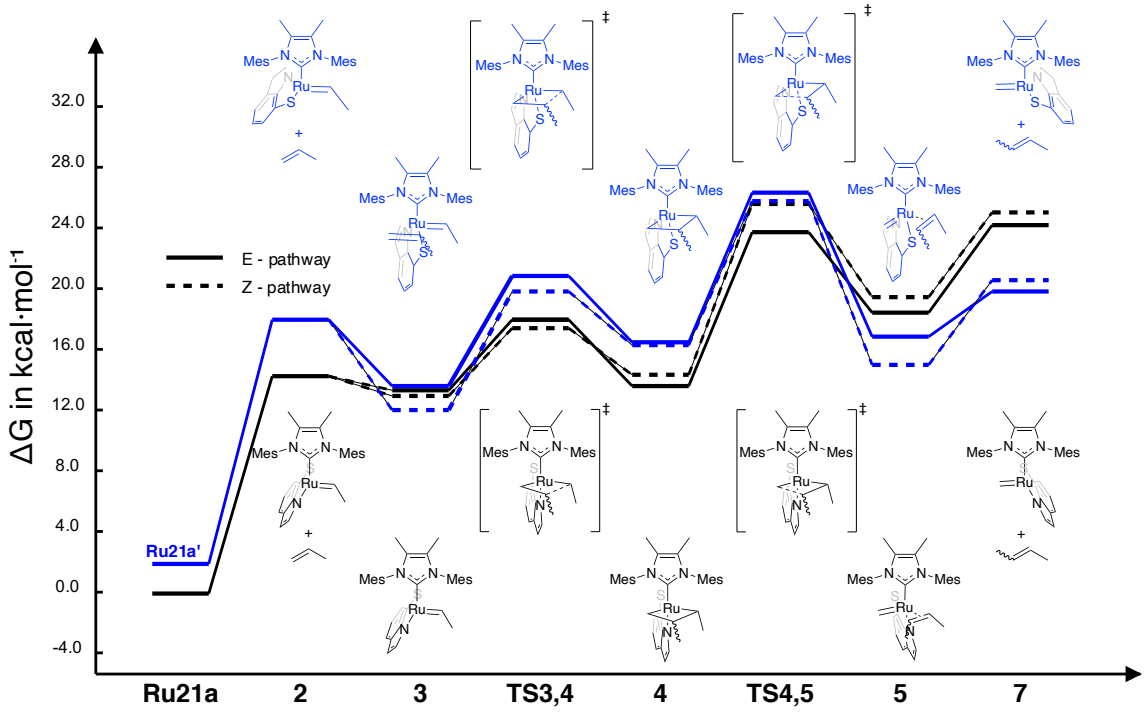

However, for the unintended isomer **Ru21a'** to be the dominating metathesis-active catalyst one of the following two requirements must be fulfilled: (i) **Ru21a** decomposes fast compared to **Ru21a'**, or (ii) the rate-determining barrier to propene metathesis using **Ru21a'** must be lower than that of **Ru21a**, so that **Ru21a'** is the dominating catalyst even in the presence of intact **Ru21a**. The extent to which either of the two requirements is fulfilled is discussed in the following:

A range of decomposition modes were investigated for **Ru21a** and **Ru21a'**, covering β-H elimination [27,28] and nucleophilic attack of the thio-indolate ligand on the alkylidene [7] during productive (Scheme S5) and non-productive metathesis (Scheme S6), regeneration of the ethylidene from the methylidene species (Scheme S7) as well as during and after the formation of the unsubstituted MCB (Scheme S8). These calculations show, in agreement with experiments, that the decomposition via β-H elimination is favorable for the unsubstituted MCB (**Ru21a_TS22,24** vs **Ru21a_TS21,23**, Scheme S8), but it becomes more difficult with an increasing number of substituents around the MCB, hampering the distortion of the MCB necessary for hydride elimination.

Scheme S5 Free Energies of Productive Propene Metathesis Calculated Relative to Ru21a and Ru2a1', respectively

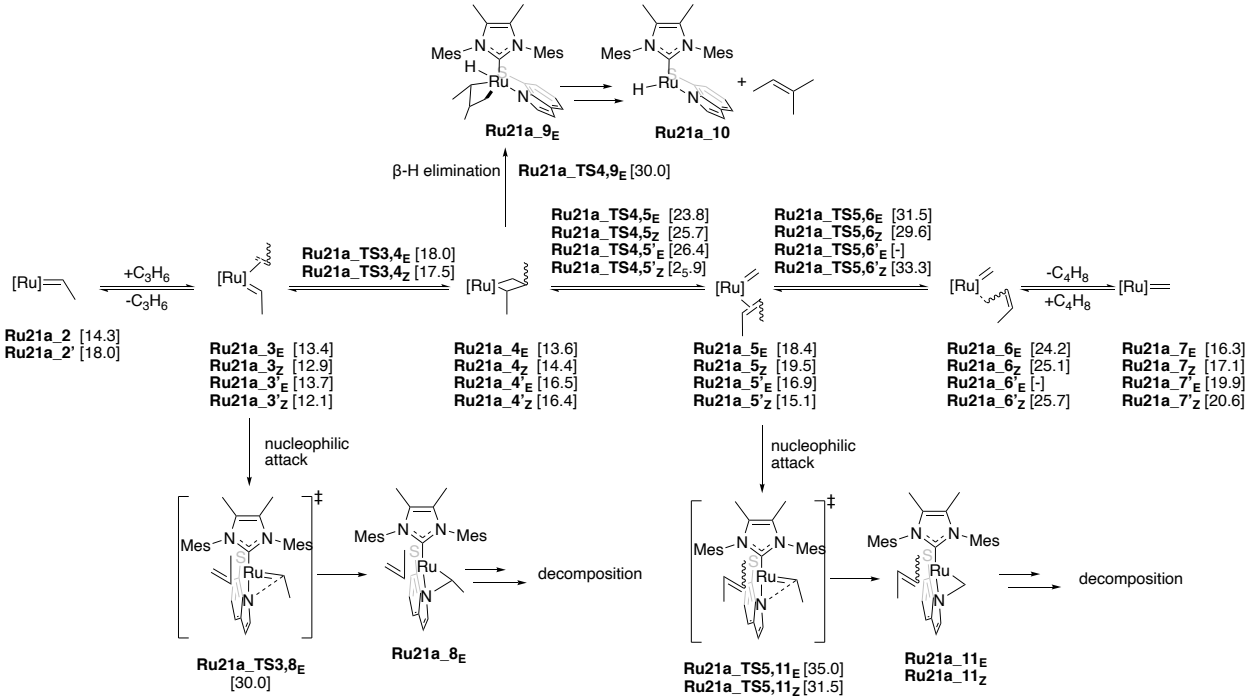

Isomers with the unintended orientation of the bidentate S,N-thio-indolate ligand (i.e., with S positioned trans to the NHC ligand) are indicated with an apostrophe ('). Isomers of the E- and Z-pathways are labeled using an E- and Z superscript suffix, respectively.

Scheme S6 Non-Productive Propene Metathesis (Ethylidene Exchange) and Associated Decomposition Reactions for Ru21a_2

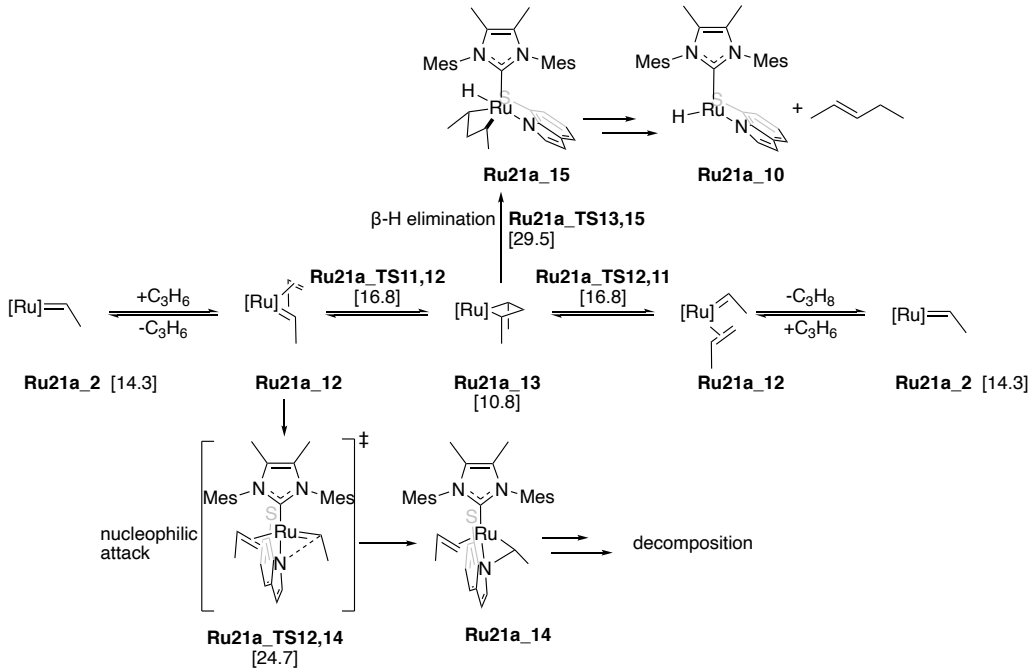

Scheme S7 Regeneration of Ru21a_2 and Ru21a_2' from Methylidene Species, and Associated Decomposition Reactions

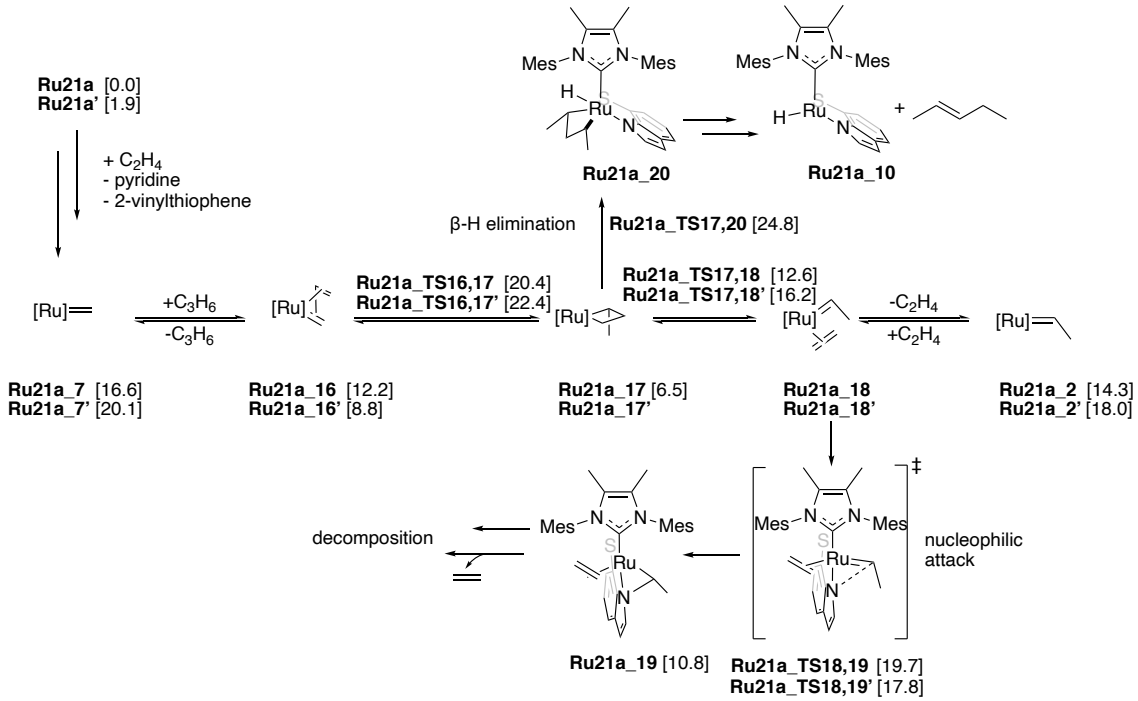

Scheme S8 Formation and Decomposition of the Unsubstituted MCB by Reacting Methylidene Ru21a_7 with Ethylene

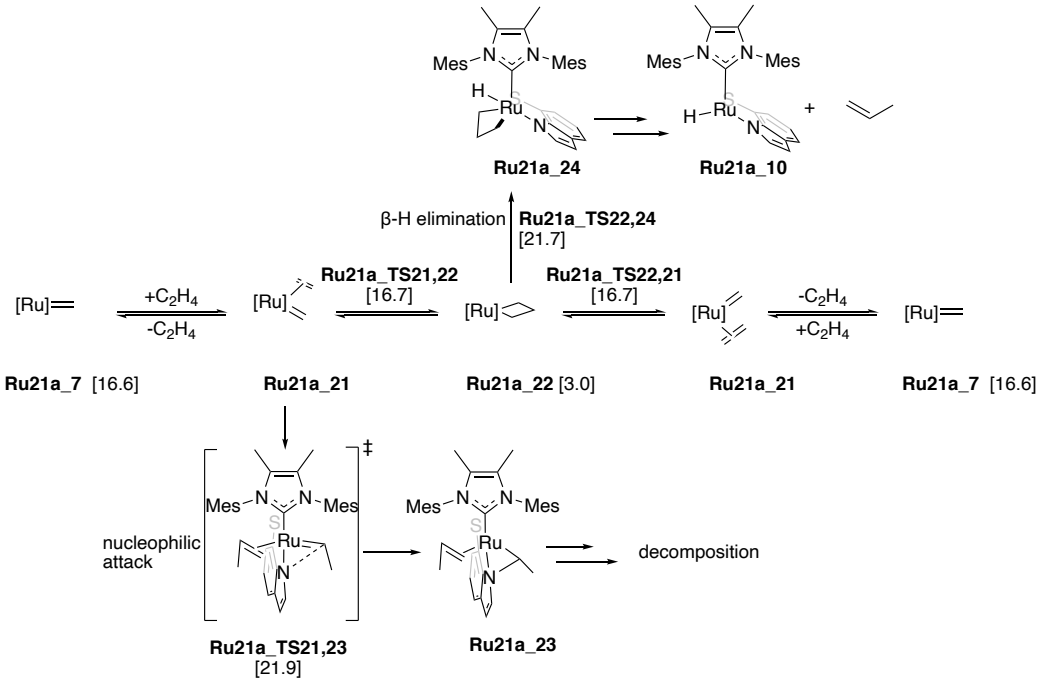

The slightly lower barrier for β-H elimination (via **Ru21a_TS21,23**) compared to that of the nucleophilic attack (via **Ru21a_TS20,22)** is consistent with propene being observed when **Ru21a** is reacted with ethylene.

For the productive and non-productive metathesis as well as for the ethylidene regeneration step, the calculations predict nucleophilic attack (via **Ru21a_TS3,8$_E$**, **Ru21a_TS5,11$_E$**, **Ru21a_TS5,11$_Z$**, **Ru21a_TS12,14** and **Ru21a_TS18,19**, Scheme S5-S8) to be the more important than β-H elimination (via **Ru21a_TS4.9$_E$** and **Ru21a_TS.24,** Scheme S5 and S8). Furthermore, nucleophilic attack via **Ru21a_TS18,19** is presumable the major decomposition pathway, since formation of **Ru21a_19** releases ethylene (Scheme S8). The free ethylene may react with a second **Ru21a_2** to form **Ru21a_18**, leading to autocatalytic decomposition of the catalyst. While this might explain the fast catalyst decomposition, it does not explain the observed Z-selectivity. With the unintended ligand orientation, the barrier to decomposition (via **Ru21a_TS18,19'**) is 1.9 kcal/mol lower than via **Ru21a_TS18,19**, and, more generally, no decomposition reaction has been found to be faster for the intended ligand orientation.

Calculations on closely related dithiolate-coordinated catalysts show that the barrier to rotation of the S,S-ligands are low (ca. 8 kcal/mol vs the 14-electron complex) [29] in four-coordinate 14-electron complexes and high in five-coordinate 16-electron complexes [5]. The observed **Ru21a**/**Ru21a'** equilibrium thus probably involves pyridine dissociation, facile ligand rotation in the four-coordinate, 14-electron complex, followed by re-binding of pyridine. Judged from the barriers to cycloreversion, the olefin metathesis pathway offered by the intended isomer **Ru21a** (with a barrier to cycloreversion $\Delta G^{\ddagger}_{TS4,5_E}$ = 23.8 kcal/mol vs **Ru21a**) is preferred, by 2.1 kcal/mol, relative to that of the unintended isomer **Ru21a'** (with a barrier to cycloreversion $\Delta G^{\ddagger}_{TS4,5'_Z}$ = 25.9 kcal/mol). Thus, if **Ru21a'** is the dominating metathesis catalyst in the mixture and responsible

for the observed Z-selectivity, another elementary step than that of cycloreversion must be rate limiting, at least for **Ru21a**. A candidate step is the dissociation of the product olefin from the π-complexes **Ru21a_5** and **Ru21a_5'** (Scheme S9). These product π-complexes are already high in energy, with a clear preference (>3 kcal/mol) for the Z-configured **Ru21a_5'$_Z$** over the E-configured **Ru21a_5$_E$**. Indeed, the dissociation of 2-butene from **Ru21_5** is rate-limiting for both **Ru21a** and **Ru21a'** (see Scheme S9).

Scheme S9 Complete Energy Profile for the Productive Metathesis of Ru21a (black) and Ru21a' (blue) with Propene Leading to (E)-2-butene (full) and (Z)-2-butene (dashed) Including the Transition State for 2-butene Dissociation

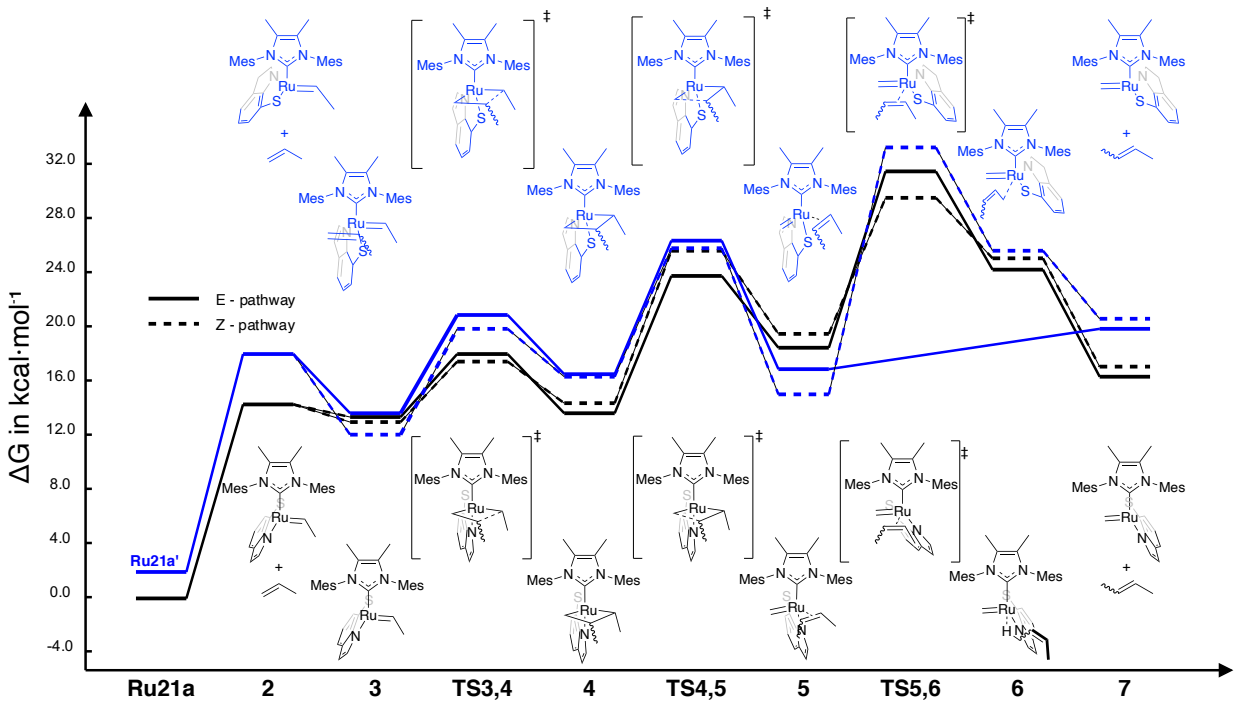

However, the DFT calculations show that the dissociation of (Z)-2-butene is favored from the intended **Ru21a** (with a barrier for dissociation of $\Delta G^{\ddagger}_{TS5,6_Z}$ = 29.6 kcal/mol vs **Ru21a**) by nearly 4 kcal/mol relative to the unintended isomer **Ru21a'** (with a barrier for dissociation of $\Delta G^{\ddagger}_{TS5,6'_Z}$ = 33.3 kcal/mol; the corresponding transition state **TS5,6'$_E$** could not be located) excluding the minor-component, unintended **Ru21a'** as an explanation for the experimentally observed Z-selectivity. Instead, the detailed DFT calculations predict **Ru21a** itself to be Z-selective. This unexpected selectivity is determined during product release, which is associated with a high barrier. This barrier thus explains both the low catalytic activity and the Z-selectivity recorded for **Ru21a**. Additionally, due to the high metathesis barrier, nucleophilic attack via **Ru21a_TS3,8** and **Ru21a_TS5,11** becomes competitive (Scheme S5), and this catalyst decomposition mode should further contribute to the low yields observed in the catalytic experiments.

Scheme S10 Initiation of Catalyst Ru21a and Ru21a' with Propene

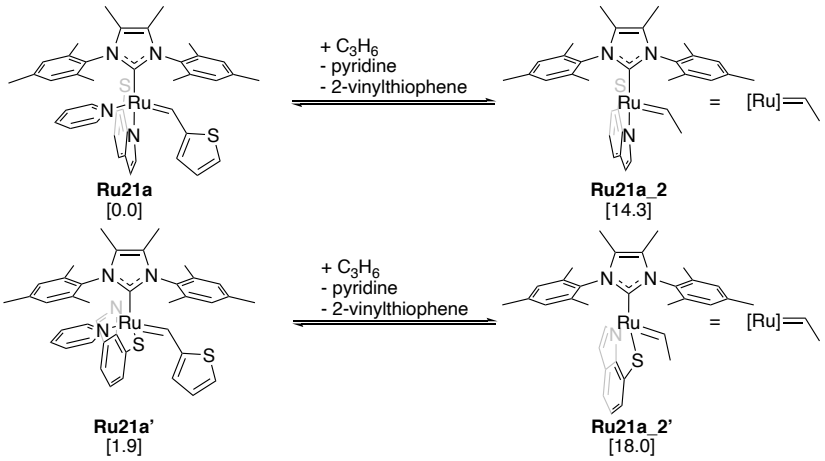

Both **Ru21a** and **Ru21a_2** are lower in energy compared to the rotamer counterpart, **Ru21a'** and **Ru21a_2'**, respectively. Therefore, we assumed that the desired orientation of the thiolate-indolate ligand should be dominant during catalysis.

Scheme S11 Decomposition of the Catalyst Precursor Ru21a and the Corresponding Pyridine-stabilized Ethylidene Species Ru21a_25 via Nucleophilic Attack of the Thio-indolate ligand on the Alkylidene

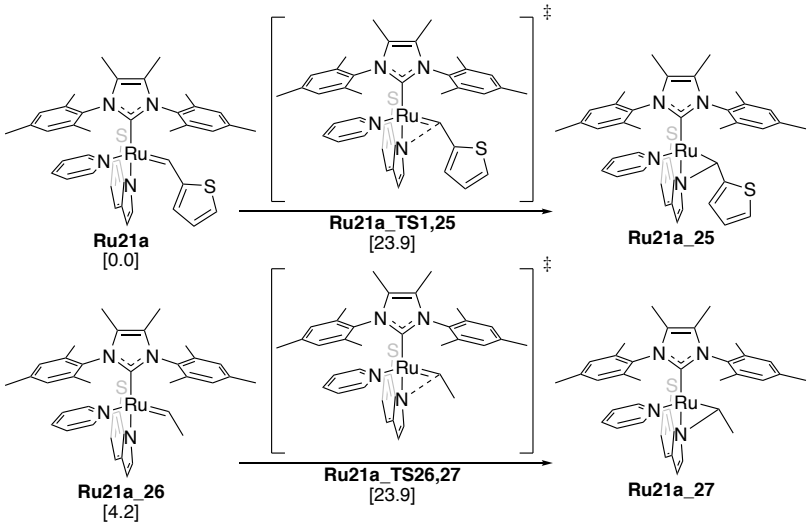

Scheme S12 Initiation and Metathesis of Ru21a with Styrene and Allylbenzene

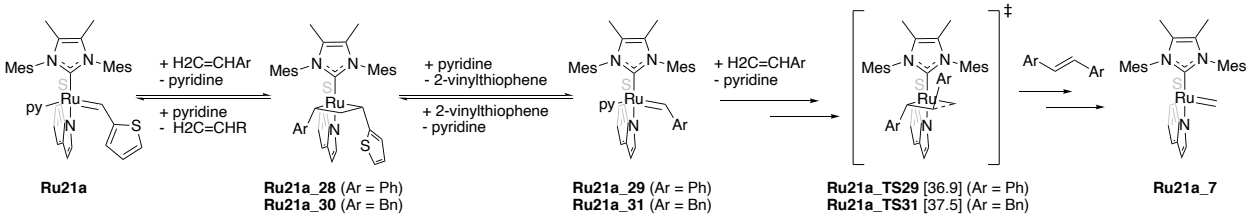

Table S7 Gibbs Free Energies of Catalyst Ru21a and Ru21a' in Olefin Metathesis (Scheme S4-12)

Model ID	$E_{\omega\mathrm{B97XD}}$ [a.u.]	$\Delta G^{T=298.15\,K}_{\omega\mathrm{B97XD},qh}$ [a.u.]	$E_{\mathrm{PBE-D3M(BJ)-PCM(benzene)}}$ [a.u.]	$\Delta G_{\mathrm{PBE-D3M(BJ)-PCM(benzene)}}$ [kcal/mol][a]
Ru21a	-2697.355932	0.664475	-2696.109762	0.0
Ru21a'	-2697.360618	0.666795	-2696.109034	1.9
Ru21a_2	-1936.599244	0.557204	-1935.685517	14.3
Ru21a_2'	-1936.596176	0.557561	-1935.679892	18.0
Ru21a_3$_E$	-2054.490362	0.639216	-2053.501974	13.4
Ru21a_3$_Z$	-2054.491931	0.639149	-2053.502621	12.9
Ru21a_3'$_E$	-2054.496890	0.641585	-2053.503787	13.7
Ru21a_3'$_Z$	-2054.498186	0.641000	-2053.505748	12.1
Ru21a_TS3,4$_E$	-2054.488530	0.640266	-2053.495739	18.0
Ru21a_TS3,4$_Z$	-2054.487601	0.639020	-2053.495251	17.5
Ru21a_TS3,4'$_E$	-2054.487845	0.641485	-2053.492400	20.8
Ru21a_TS3,4'$_Z$	-2054.487962	0.640969	-2053.493519	19.8
Ru21a_4$_E$	-2054.504418	0.643615	-2053.505965	13.6
Ru21a_4$_Z$	-2054.501219	0.642821	-2053.504033	14.4
Ru21a_4'$_E$	-2054.503723	0.644210	-2053.501999	16.5
Ru21a_4'$_Z$	-2054.502650	0.644755	-2053.502665	16.4
Ru21a_TS4,5$_E$	-2054.477152	0.639007	-2053.485211	23.8
Ru21a_TS4,5$_Z$	-2054.472273	0.637626	-2053.480792	25.7
Ru21a_TS4,5'$_E$	-2054.478071	0.641170	-2053.483118	26.4
Ru21a_TS4,5'$_Z$	-2054.478310	0.640906	-2053.483663	25.9
Ru21a_5$_E$	-2054.483160	0.640503	-2053.495232	18.4
Ru21a_5$_Z$	-2054.482927	0.640123	-2053.493143	19.5
Ru21a_5'$_E$	-2054.489193	0.641082	-2053.498174	16.9
Ru21a_5'$_Z$	-2054.492602	0.640976	-2053.500928	15.1
Ru21a_TS5,6$_E$	-2054.468797	0.636473	-2053.470428	31.5
Ru21a_TS5,6$_Z$	-2054.472557	0.634588	-2053.471556	29.6
Ru21a_TS5,6'$_E$	-	-	-	-
Ru21a_TS5,6'$_Z$	-2054.468627	0.634813	-2053.465778	33.3
Ru21a_6$_E$	-2054.477492	0.635618	-2053.481121	24.2
Ru21a_6$_Z$	-2054.478311	0.636813	-2053.480974	25.1

Ru21a_6'$_E$	-	-	-	-
Ru21a_6'$_Z$	-2054.477038	0.636062	-2053.47924	25.7
Ru21a_7	-1897.284227	0.530006	-1896.398580	16.6
Ru21a_7'	-1897.280929	0.530301	-1896.393209	20.1
Ru21a_7$_E$	-1897.284227	0.530006	-1896.398580	16.3
Ru21a_7$_Z$	-1897.284227	0.530006	-1896.398580	17.1
Ru21a_7'$_E$	-1897.280929	0.530301	-1896.393209	19.9
Ru21a_7'$_Z$	-1897.280929	0.530301	-1896.393209	20.6
Ru21a_TS4,9$_E$	-2054.473604	0.641711	-2053.478065	30.0
Ru21a_TS3,8$_E$	-2054.466387	0.640816	-2053.477110	30.0
Ru21a_TS5,11$_E$	-2054.456933	0.639644	-2053.467883	35.0
Ru21a_ TS5,11$_Z$	-2054.461372	0.638397	-2053.472248	31.5
Ru21a_TS12,13	-2054.490549	0.640213	-2053.497524	16.8
Ru21a_13	-2054.507086	0.642073	-2053.509008	10.8
Ru21a_TS12,14	-2054.473914	0.639050	-2053.483851	24.7
Ru21a_TS13,15	-2054.471277	0.641354	-2053.478453	29.5
Ru21a_16	-2015.180436	0.613642	-2014.222266	12.2
Ru21a_16'	-2015.190804	0.614203	-2014.228295	8.8
Ru21a_TS16,17	-2015.171824	0.613631	-2014.209193	20.4
Ru21a_TS16,17'	-2015.172348	0.614061	-2014.206856	22.1
Ru21a_17	-2015.200702	0.615084	-2014.232697	6.5
Ru21a_TS17,18	-2015.183260	0.612693	-2014.220658	12.6
Ru21a_TS17,18'	-2015.181467	0.613576	-2014.215818	16.2
Ru21a_TS18,19	-2015.170107	0.612650	-2014.209362	19.7
Ru21a_TS18,19'	-2015.177554	0.614086	-2014.213688	17.8
Ru21a_19	-2015.202320	0.616426	-2014.227241	10.8
Ru21a_TS17,20	-2015.167037	0.612748	-2014.201205	24.8
Ru21a_TS21,22	-1975.862161	0.585097	-1974.930482	16.7
Ru21a_22	-1975.893731	0.588854	-1974.956018	3.0
Ru21a_TS21,23	-1975.851195	0.584605	-1974.921696	21.9
Ru21a_TS22,24	-1975.855492	0.584776	-1974.922133	21.7
Ru21a_TS1,25	-2697.322853	0.664852	-2696.072076	23.9
Ru21_26	-2184.852578	0.646098	-2183.814011	4.2
Ru21a_TS26,27	-2184.821662	0.645454	-2183.782032	23.9
Ru21a_TS29	-2437.859282	0.742683	-2436.665841	36.9
Ru21a_TS31	-2516.469924	0.798578	-2515.215479	37.5
Vinylthiophene	-630.360711	0.069869	-630.076561	-
Pyridine	-248.211971	0.062066	-248.088721	-
Styrene	-309.557280	0.103658	-309.388691	-
Allylbenzene	-348.530228	0.124270	-348.654961	-

a Relative to **Ru21a**

S4. NMR Spectra.

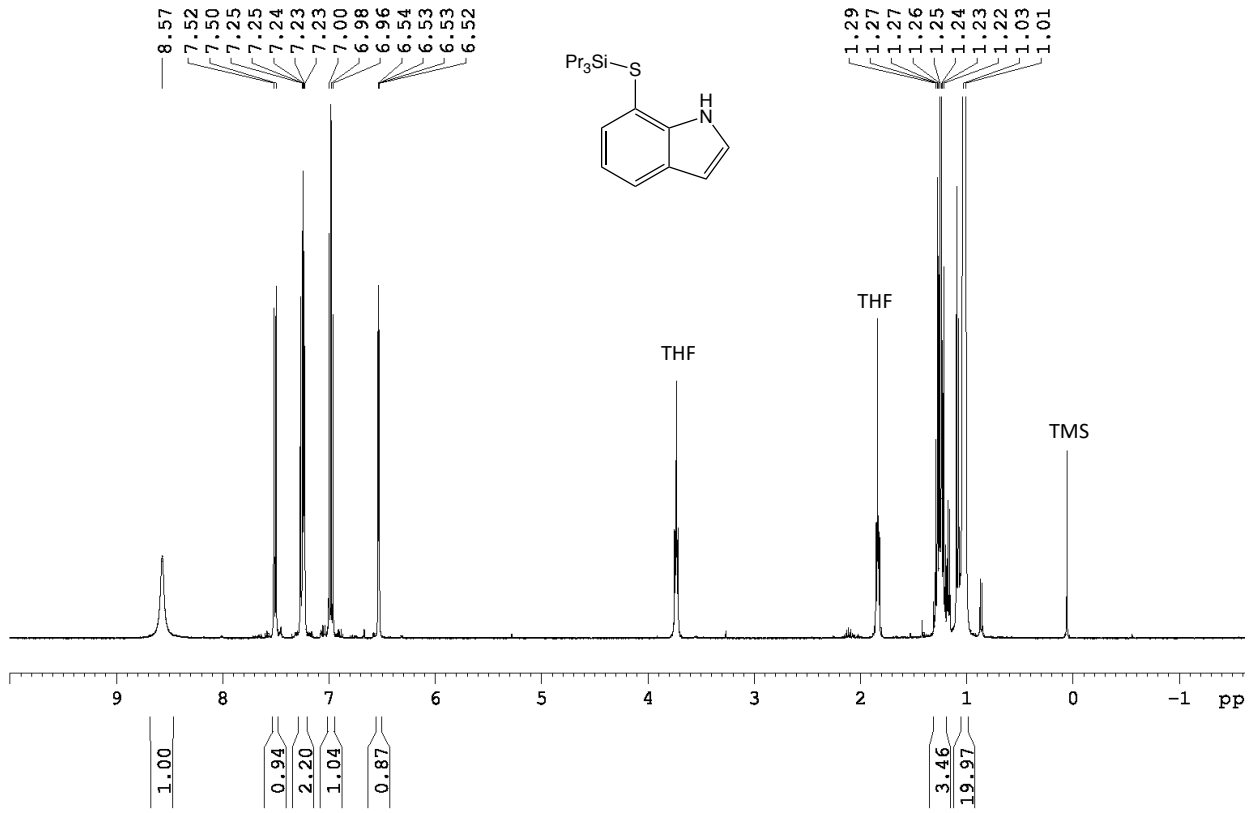

Fig. S11 1H NMR spectrum of **L2a**. Solvent impurities are indicated in the spectrum (CDCl3, 300.1 MHz)

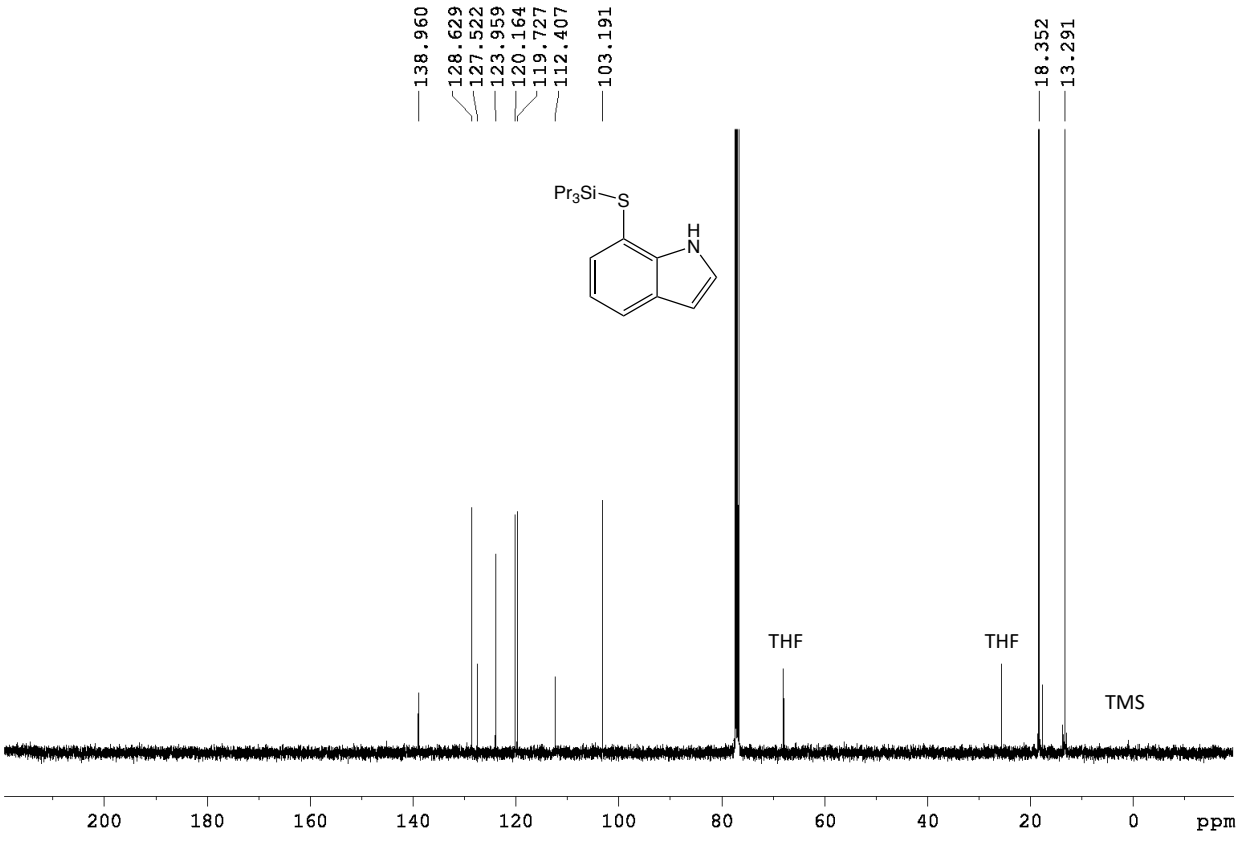

Fig. S12 ^{13}C NMR spectrum of **L2a** ($CDCl_3$, 300.1 MHz)

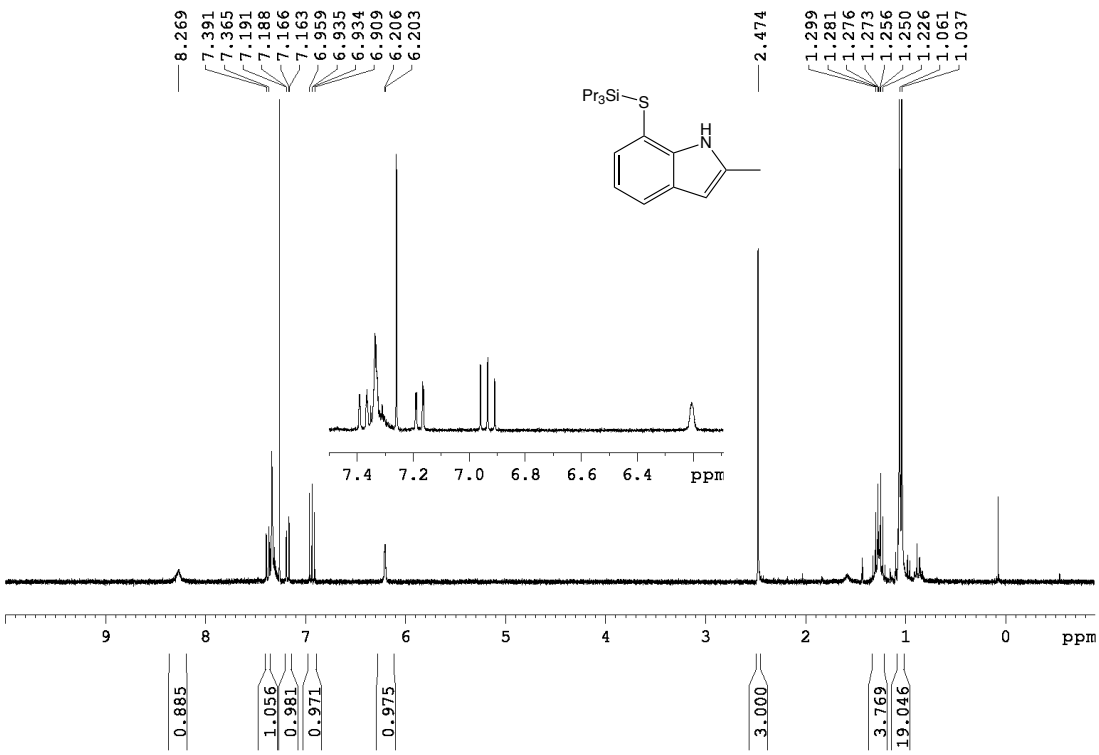

Fig. S13 ^{1}H NMR spectrum of **L2b** ($CDCl_3$, 300.1 MHz)

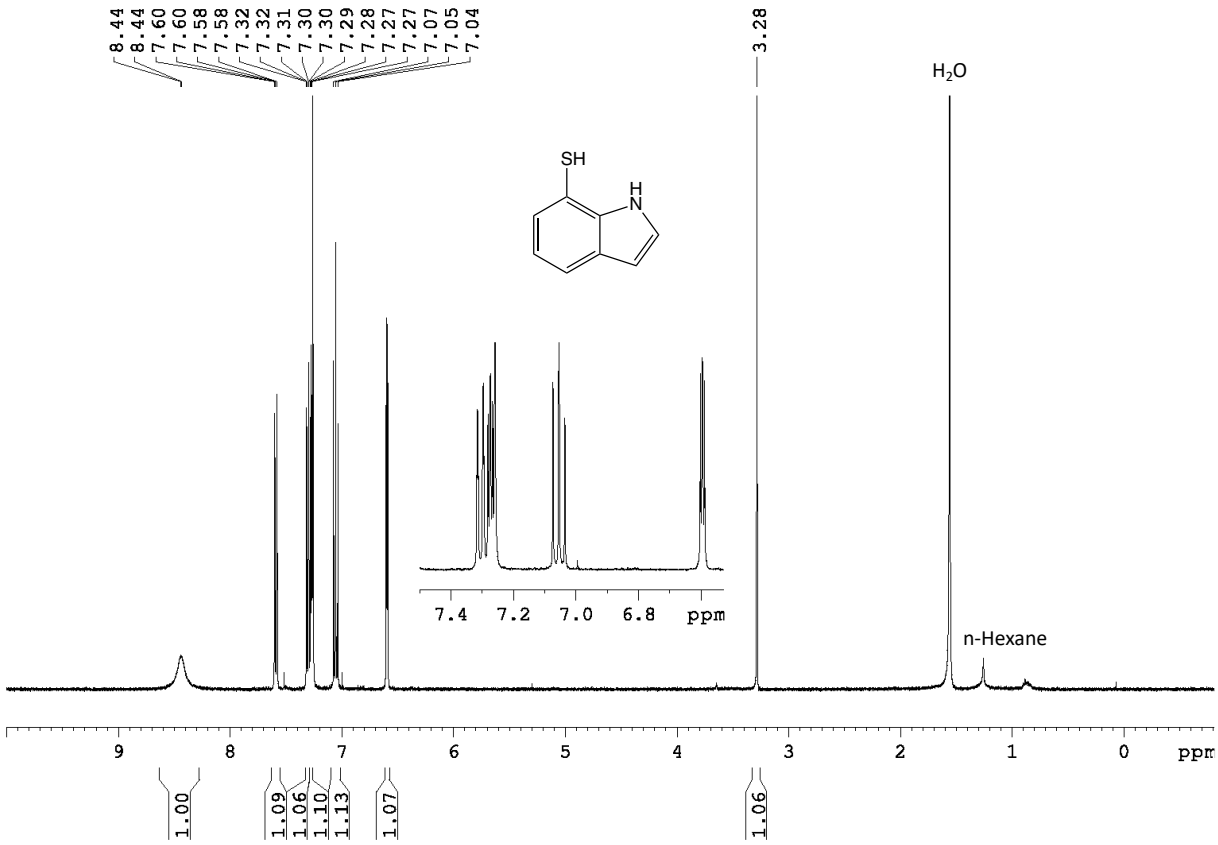

Fig. S14 ^{1}H NMR spectrum of **L3a** ($CDCl_3$, 300.1 MHz)

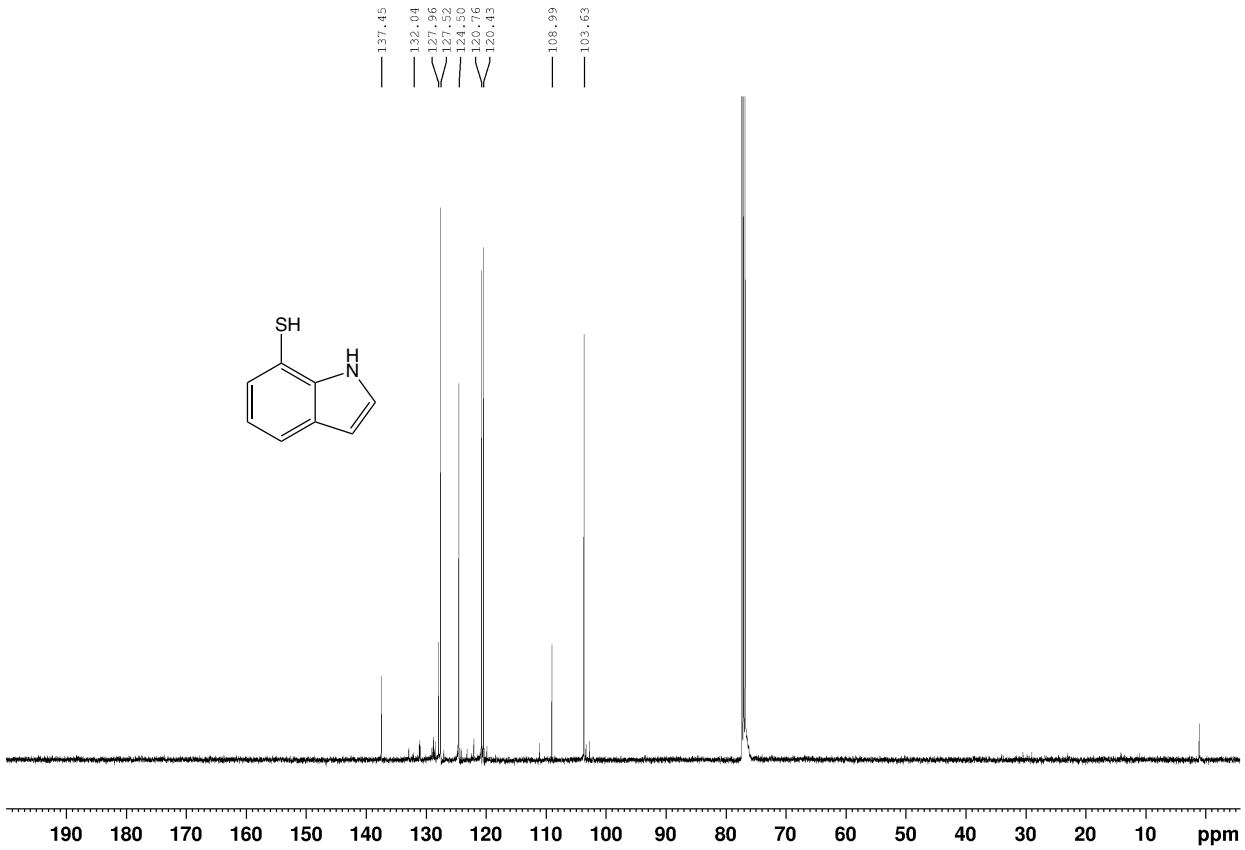

Fig. S15 ^{13}C NMR spectrum of **L3a** ($CDCl_3$, 300.1 MHz)

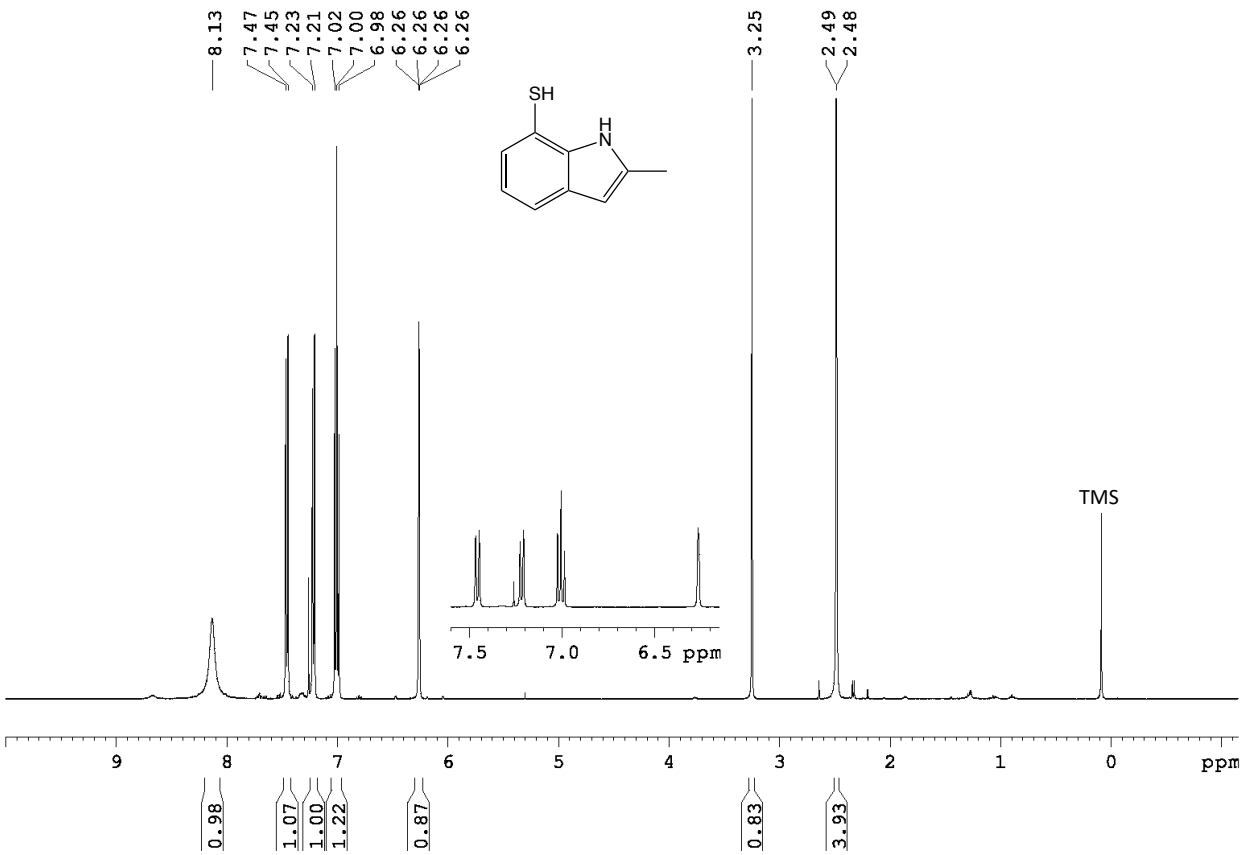

Fig. S16 ^{1}H NMR spectrum of **L3b** ($CDCl_3$, 300.1 MHz)

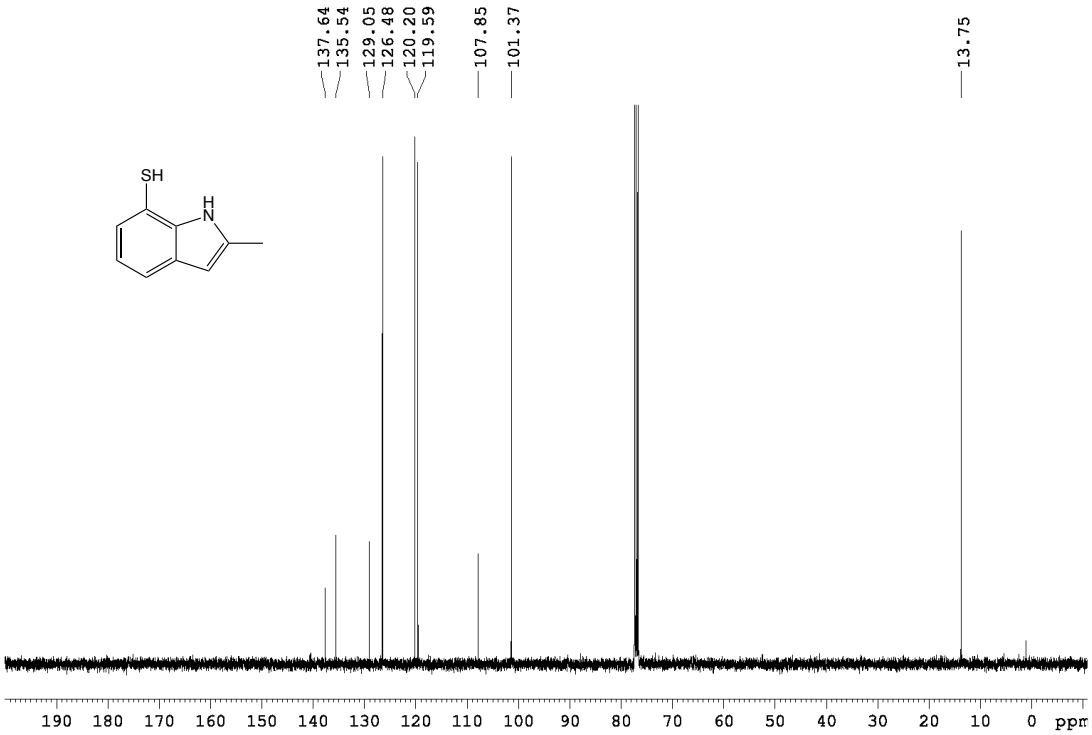

Fig. S17 ^{13}C NMR spectrum of **L3b** ($CDCl_3$, 300.1 MHz)

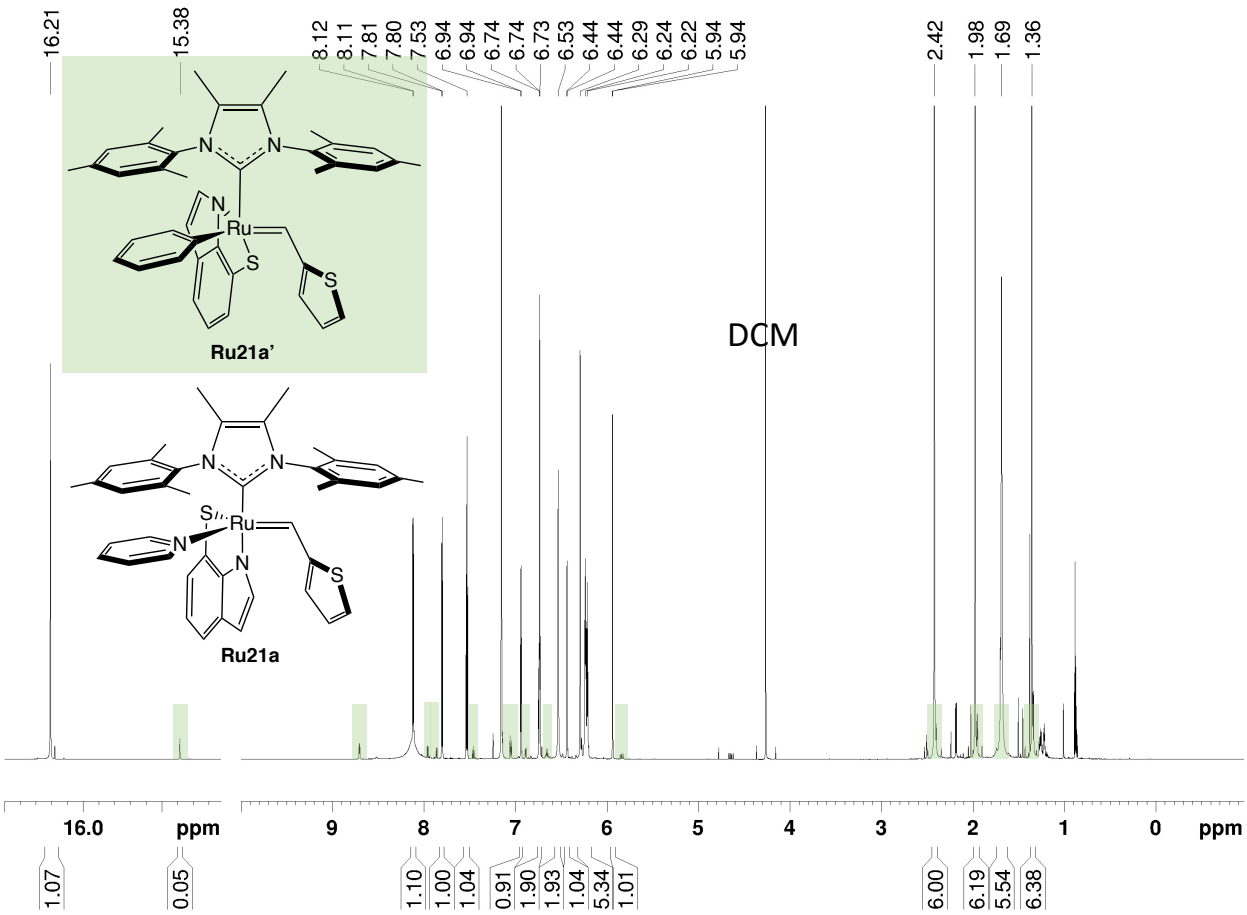

Fig. S18 ^{1}H NMR spectrum of **Ru21a** and **Ru21a'** (C_6D_6, 850 MHz)

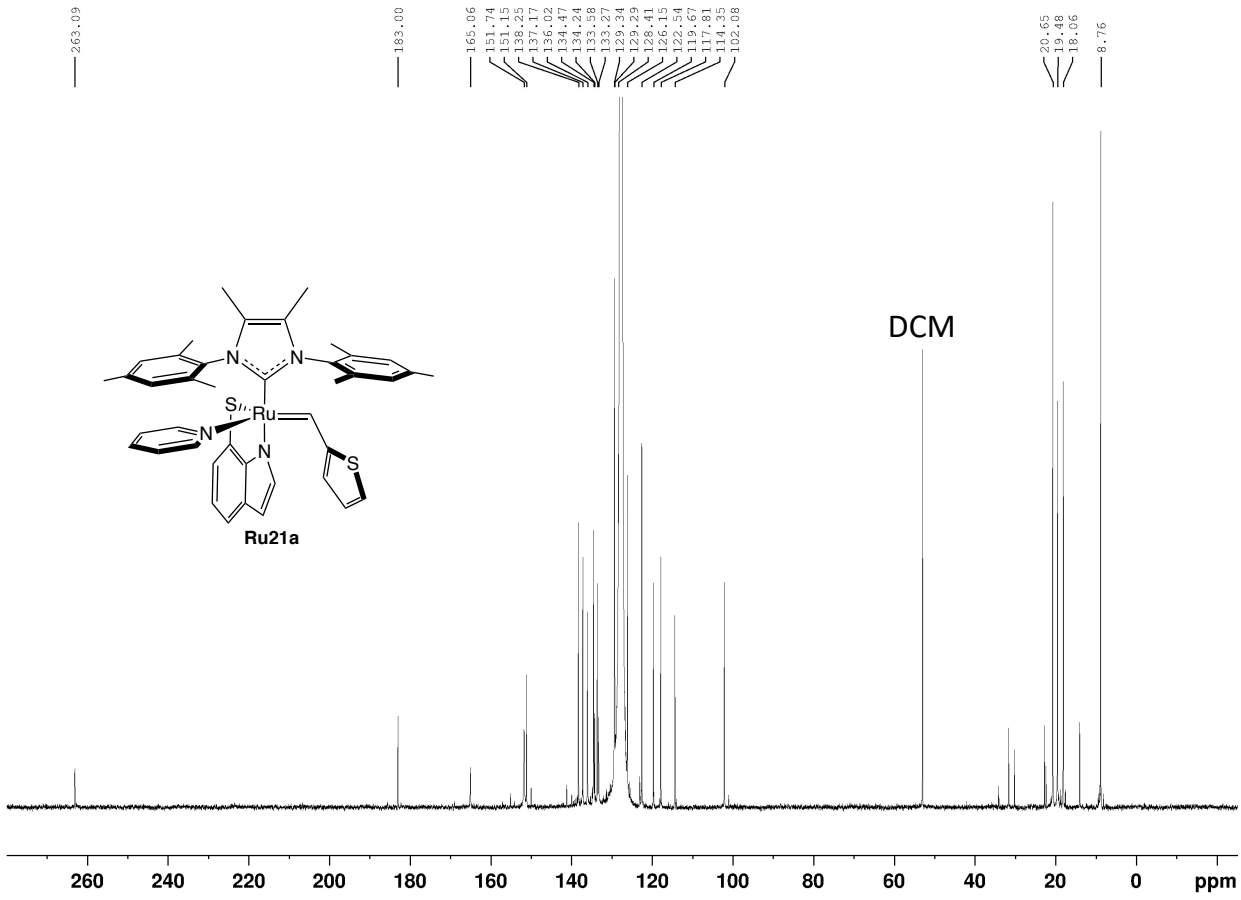

Fig. S19 ^{13}C NMR spectrum of **Ru21a** (C_6D_6, 850 MHz)

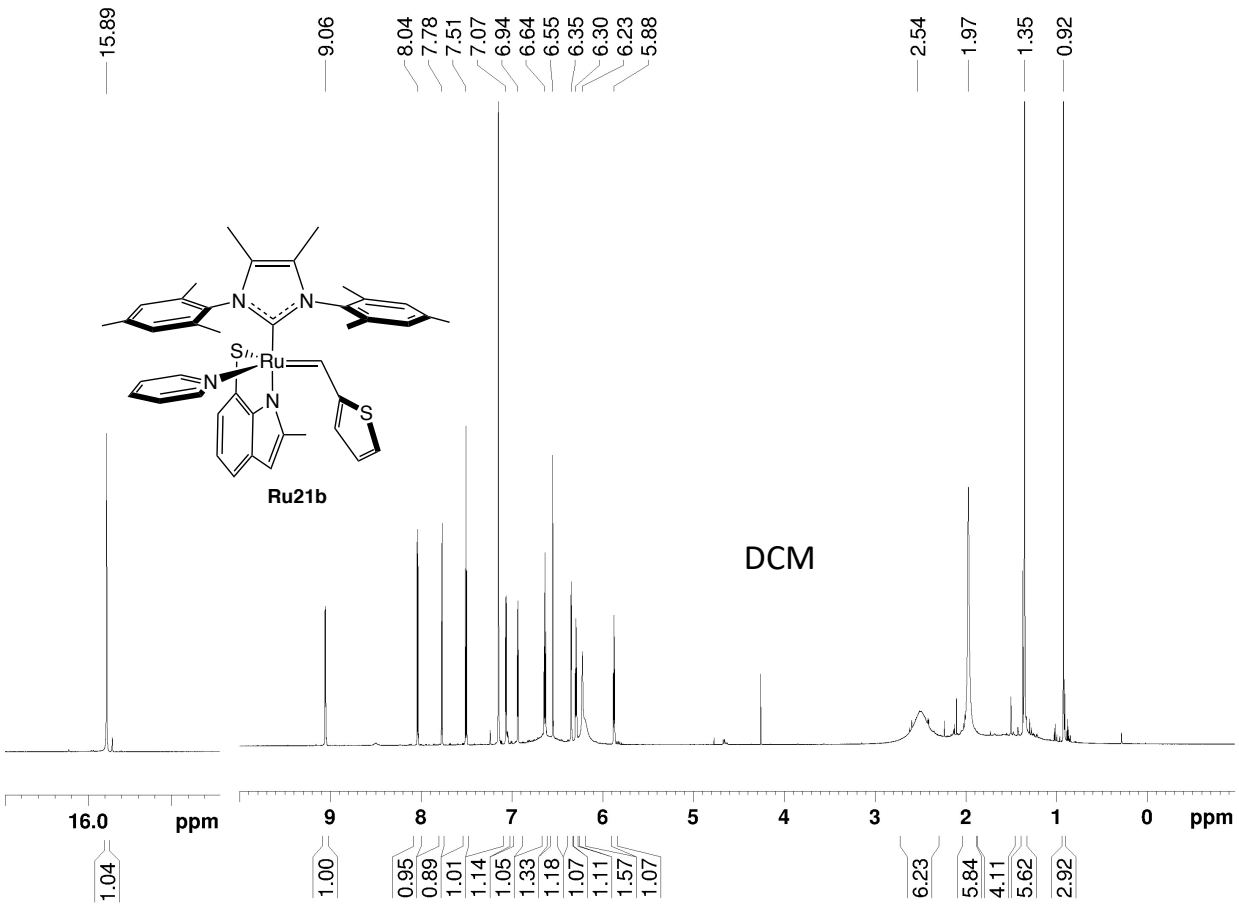

Fig. S20 ^{1}H NMR spectrum of **Ru21b** (C_6D_6, 500 MHz)

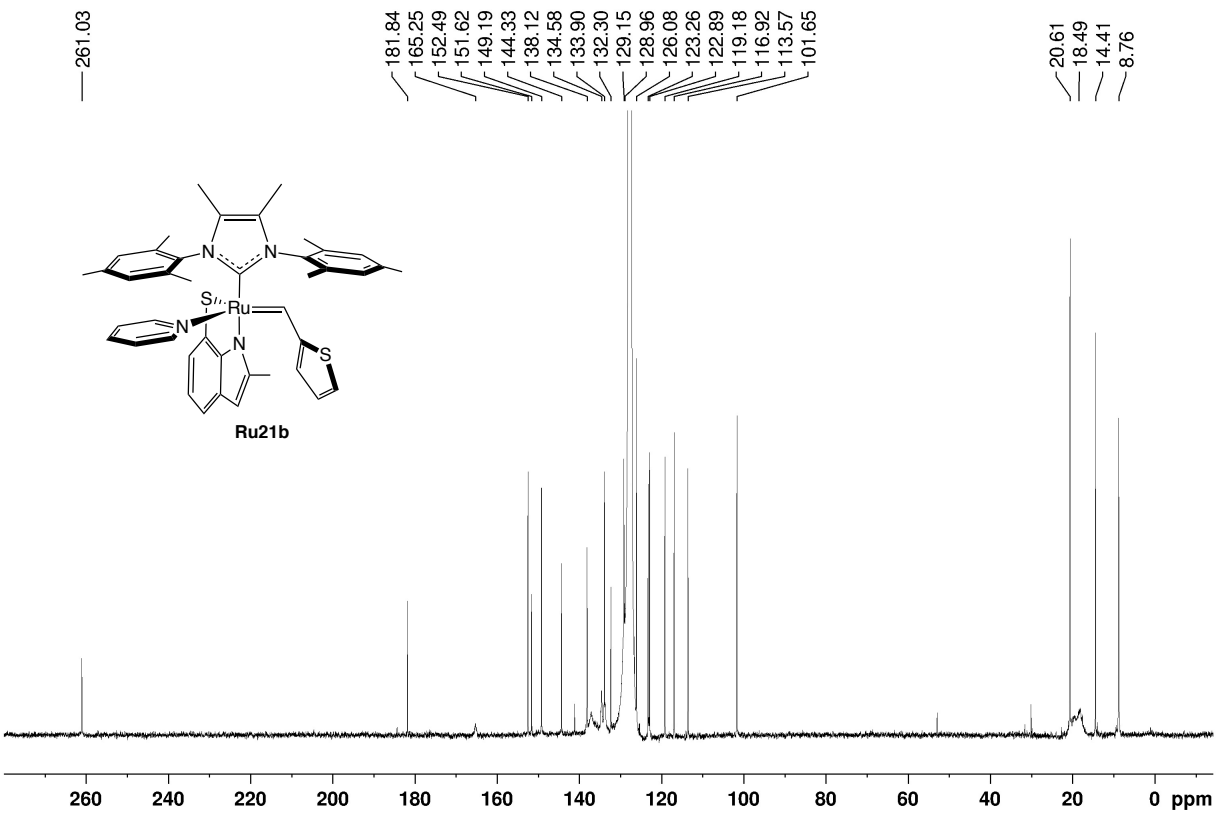

Fig. S21 ^{13}C NMR spectrum of **Ru21b** (C_6D_6, 850 MHz)

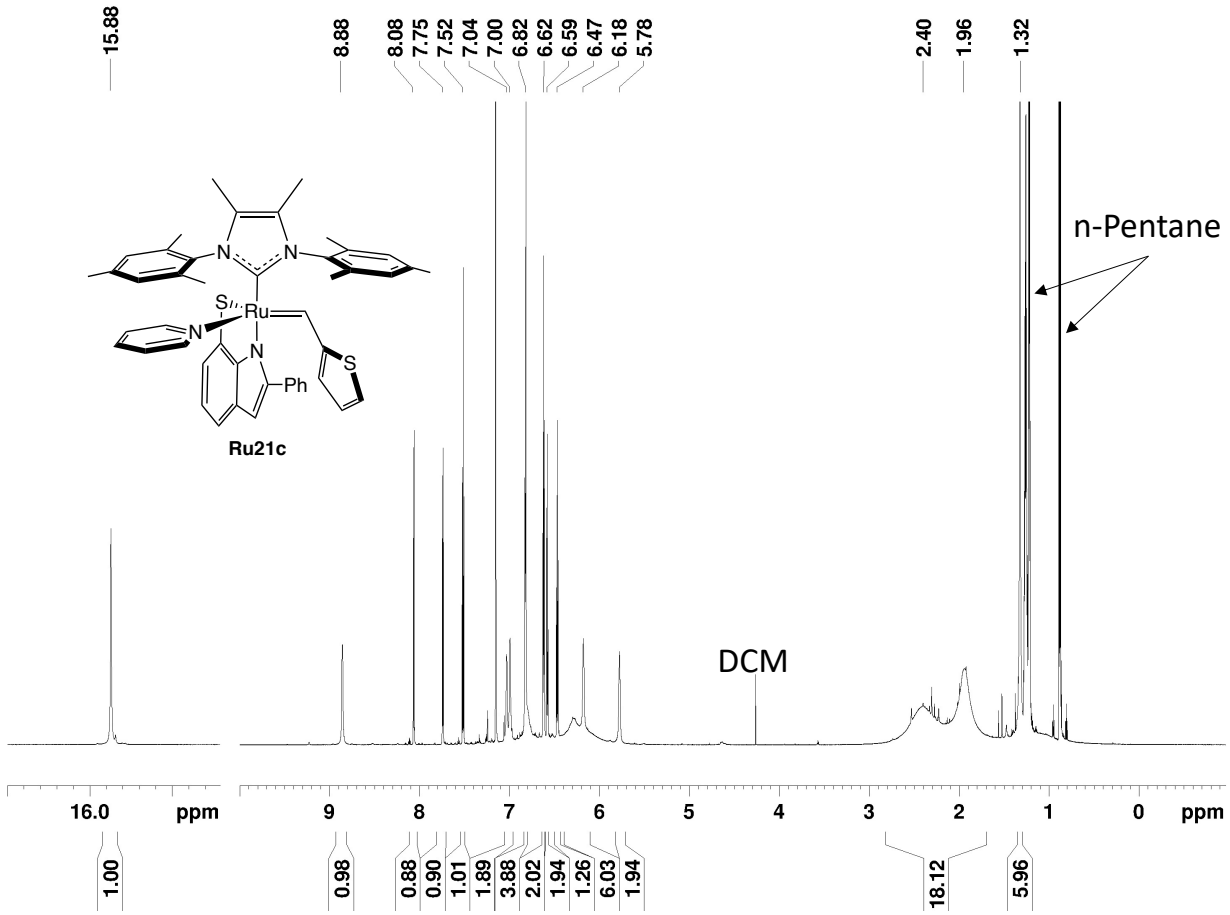

Fig. S22 ^{1}H NMR spectrum of **Ru21c** (C_6D_6, 850 MHz)

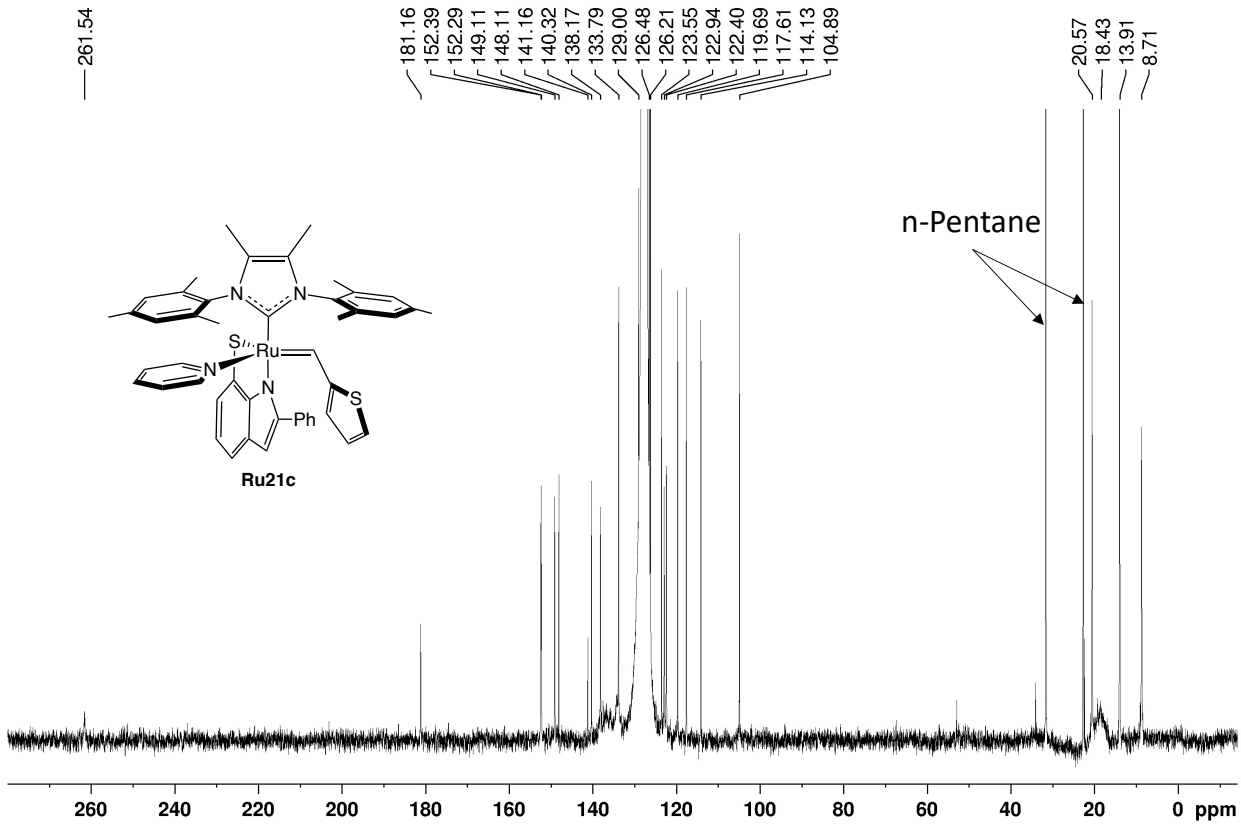

Fig. S23 ^{13}C NMR spectrum of **Ru21c** (C_6D_6, 850 MHz)

S5. X-ray Crystal Structures

Data collection on compound **Ru21a** was done on beamline BM01 at the Swiss-Norwegian Beamlines at the ESRF synchrotron in Grenoble, France, using Si double-mirror monochromated radiation (λ = 0.62379 Å) applying a 360-degree phi-scan and a Pilatus2M detector. The technical assistance of the Dr. Dmitry Chernyshov, and the SNBL at the ESRF is gratefully acknowledged.

X-ray Crystal Structure of Ru21a

X-Ray suitable crystal were obtained by layering a concentrated DCM solution of **Ru21a** with pentane at -30 °C. The quality of the obtained crystals was good for proof of connectivity, but not for qualitative comparison. The thiophene group is rotationally disordered.

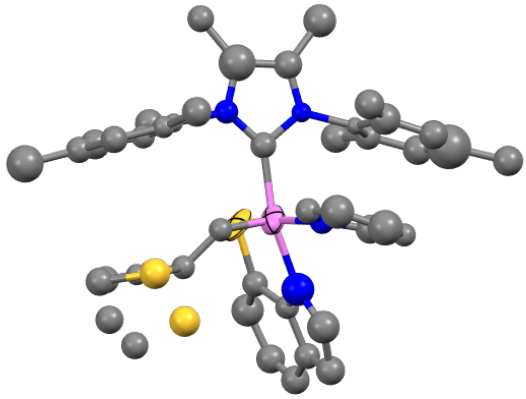

Fig. S24 X-ray crystal structure of **Ru21a**, with displacement ellipsoids drawn at 50% probability. The Ruthenium is shown in violet, sulfur in yellow, nitrogen in blue, and carbon in gray. Hydrogen atoms have been omitted for clarity.

Table S8: Crystal Data and Structure Refinement for Ru21a

Identification code	**Ru21a**	
Empirical formula	C41 H42 N4 Ru S2 + Solvents	
Formula weight	755.97	
Temperature	200(2) K	
Wavelength	0.62379 Å	
Crystal system	Orthorhombic	
Space group	Pbca	
Unit cell dimensions	a = 19.596(3) Å	α= 90°.
	b = 19.404(4) Å	β= 90°.
	c = 22.551(7) Å	γ = 90°.
Volume	8575(3) $Å^3$	
Z	8	

Density (calculated)	1.171 Mg/m^3
Absorption coefficient	0.344 mm^{-1}
F(000)	3136
Crystal size	0.11 x 0.04 x 0.01 mm^3
Theta range for data collection	1.585 to 16.469°.
Index ranges	-15<=h<=15, -17<=k<=17, -20<=l<=20
Reflections collected	20069
Independent reflections	3222 [R(int) = 0.3880]
Completeness to theta = 16.469°	95.8 %
Absorption correction	Semi-empirical from equivalents
Max. and min. transmission	1.00000 and 0.73091
Refinement method	Full-matrix least-squares on F^2
Data / restraints / parameters	3222 / 11 / 224
Goodness-of-fit on F^2	1.167
Final R indices [I>2sigma(I)]	R1 = 0.1788, wR2 = 0.3671
R indices (all data)	R1 = 0.2459, wR2 = 0.4044
Extinction coefficient	n/a
Largest diff. peak and hole	0.764 and -0.630 $e.Å^{-3}$

X-ray Crystal Structure of Ru21c

X-Ray suitable crystal were obtained by layering a concentrated toluene solution of **Ru21c** with pentane at -30 °C. The thiophene group is rotationally disordered.

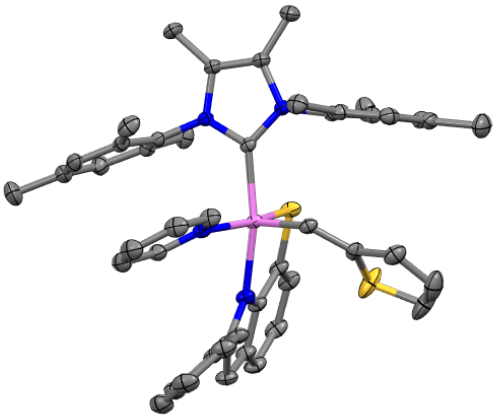

Fig. S25 X-ray crystal structure of **Ru21c**, with displacement ellipsoids drawn at 50% probability. Ruthenium is shown in violet, sulfur in yellow, nitrogen in blue, and carbon in gray. Hydrogen atoms have been omitted for clarity

Table S9: Crystal Data and Structure Refinement for Ru21c

Identification code	**Ru21c** (CCDC: 2086885)	
Empirical formula	C55.50 H62 N4 Ru S2	
Formula weight	950.28	
Temperature	123(2) K	
Wavelength	0.71073 Å	
Crystal system	Triclinic	
Space group	P-1	
Unit cell dimensions	a = 10.9904(8) Å	α= 94.1084(11)°.
	b = 14.3209(11) Å	β= 100.7967(11)°.
	c = 16.6513(12) Å	γ = 111.5795(10)°.
Volume	2365.4(3) $Å^3$	
Z	2	
Density (calculated)	1.334 Mg/m^3	
Absorption coefficient	0.462 mm^{-1}	
F(000)	998	
Crystal size	0.682 x 0.379 x 0.052 mm^3	
Theta range for data collection	1.548 to 32.023°.	
Index ranges	-16<=h<=16, -21<=k<=21, -24<=l<=24	

Reflections collected	45464
Independent reflections	16392 [R(int) = 0.0863]
Completeness to theta = 25.242°	100.0 %
Absorption correction	Semi-empirical from equivalents
Max. and min. transmission	0.95801 and 0.72930
Refinement method	Full-matrix least-squares on F^2
Data / restraints / parameters	16392 / 591 / 615
Goodness-of-fit on F^2	1.041
Final R indices [I>2sigma(I)]	R1 = 0.0451, wR2 = 0.1234
R indices (all data)	R1 = 0.0509, wR2 = 0.1273
Extinction coefficient	n/a
Largest diff. peak and hole	1.860 and -0.902 e.$Å^{-3}$

S6. References

1. Fulmer GR, Miller AJM, Sherden NH, Gottlieb HE, Nudelman A, Stoltz BM, Bercaw JE, Goldberg KI (2010) NMR Chemical Shifts of Trace Impurities: Common Laboratory Solvents, Organics, and Gases in Deuterated Solvents Relevant to the Organometallic Chemist. Organometallics 29:2176-2179. https://doi.org/10.1021/om100106e
2. Lummiss JAM, Oliveira KC, Pranckevicius A, Santos A, dos Santos EN, Fogg DE (2012) Chemical Plants: High-Value Molecules from Essential Oils. J Am Chem Soc 134:18889–18891
3. Blacquiere JM, Jurca T, Weiss J, Fogg DE (2008) Time as a Dimension in High-Throughput Homogeneous Catalysis. Adv Synth Catal 350:2849-2855. https://doi.org/10.1002/adsc.200800596
4. Occhipinti G, Törnroos KW, Jensen VR (2017) Pyridine-Stabilized Fast-Initiating Ruthenium Monothiolate Catalysts for Z-Selective Olefin Metathesis. Organometallics 36:3284-3292. https://doi.org/10.1021/acs.organomet.7b00441
5. Mikus MS, Torker S, Xu C, Li B, Hoveyda AH (2016) Pentacoordinate Ruthenium(II) Catecholthiolate and Mercaptophenolate Catalysts for Olefin Metathesis: Anionic Ligand Exchange and Ease of Initiation. Organometallics 35:3878-3892. https://doi.org/10.1021/acs.organomet.6b00773
6. Waser J, Gaspar B, Nambu H, Carreira EM (2006) Hydrazines and azides via the metal-catalyzed hydrohydrazination and hydroazidation of olefins. J Am Chem Soc 128:11693-11712. https://doi.org/10.1021/ja062355+
7. Koh MJ, Khan RK, Torker S, Yu M, Mikus MS, Hoveyda AH (2015) High-value alcohols and higher-oxidation-state compounds by catalytic Z-selective cross-metathesis. Nature 517:181-186. https://doi.org/10.1038/nature14061
8. Watanabe R, Sugai C, Yamazaki T, Matsushima R, Uchida H, Matsumiya M, Takatsu A, Suzuki T (2016) Quantitative Nuclear Magnetic Resonance Spectroscopy Based on PULCON Methodology: Application to Quantification of Invaluable Marine Toxin, Okadaic Acid. Toxins (Basel) 8. https://doi.org/10.3390/toxins8100294
9. Smit W, Ekeli JB, Occhipinti G, Woźniak B, Törnroos KW, Jensen VR (2020) Z-Selective Monothiolate Ruthenium Indenylidene Olefin Metathesis Catalysts. Organometallics 39:397-407. https://doi.org/10.1021/acs.organomet.9b00641
10. Frisch MJ, Trucks GW, Schlegel HB, Scuseria GE, Robb MA, Cheeseman JR, Scalmani G, Barone V, Petersson GA, Nakatsuji H, Li X, Caricato M, Marenich AV, Bloino J, Janesko BG, Gomperts R, Mennucci B, Hratchian HP, Ortiz JV, Izmaylov AF, Sonnenberg JL, Williams, Ding F, Lipparini F, Egidi F, Goings J, Peng B, Petrone A, Henderson T, Ranasinghe D, Zakrzewski VG, Gao J, Rega N, Zheng G, Liang W, Hada M, Ehara M, Toyota K, Fukuda R, Hasegawa J, Ishida M, Nakajima T, Honda Y, Kitao O, Nakai H, Vreven T, Throssell K, Montgomery Jr. JA, Peralta JE, Ogliaro F, Bearpark MJ, Heyd JJ, Brothers EN, Kudin KN, Staroverov VN, Keith TA, Kobayashi R, Normand J, Raghavachari K, Rendell AP, Burant JC, Iyengar SS, Tomasi J, Cossi M, Millam JM, Klene M, Adamo C, Cammi R, Ochterski JW, Martin RL, Morokuma K, Farkas O, Foresman JB, Fox DJ. Gaussian 16 Rev. C.01: Wallingford, CT, 2016
11. Perdew JP, Burke K, Ernzerhof M (1996) Generalized Gradient Approximation Made Simple. Phys Rev Lett 77:3865-3868. https://doi.org/10.1103/PhysRevLett.77.3865
12. Chai JD, Head-Gordon M (2008) Long-range corrected hybrid density functionals with damped atom-atom dispersion corrections. Phys Chem Chem Phys 10:6615-6620. https://doi.org/10.1039/b810189b

13. Zhao Y, Truhlar DG (2006) A new local density functional for main-group thermochemistry, transition metal bonding, thermochemical kinetics, and noncovalent interactions. J Chem Phys 125:194101. https://doi.org/10.1063/1.2370993
14. Zhao Y, Truhlar DG (2008) Density functionals with broad applicability in chemistry. Acc Chem Res 41:157-167. https://doi.org/10.1021/ar700111a
15. Ribeiro RF, Marenich AV, Cramer CJ, Truhlar DG (2011) Use of solution-phase vibrational frequencies in continuum models for the free energy of solvation. J Phys Chem B 115:14556-14562. https://doi.org/10.1021/jp205508z
16. Grimme S, Ehrlich S, Goerigk L (2011) Effect of the damping function in dispersion corrected density functional theory. J Comput Chem 32:1456-1465. https://doi.org/10.1002/jcc.21759
17. Smith DG, Burns LA, Patkowski K, Sherrill CD (2016) Revised Damping Parameters for the D3 Dispersion Correction to Density Functional Theory. J Phys Chem Lett 7:2197-2203. https://doi.org/10.1021/acs.jpclett.6b00780
18. Peterson KA, Figgen D, Dolg M, Stoll H (2007) Energy-consistent relativistic pseudopotentials and correlation consistent basis sets for the 4d elements Y-Pd. J Chem Phys 126:124101. https://doi.org/10.1063/1.2647019
19. Dunning TH (1989) Gaussian basis sets for use in correlated molecular calculations. I. The atoms boron through neon and hydrogen. J Chem Phys 90:1007-1023. https://doi.org/10.1063/1.456153
20. Schuchardt KL, Didier BT, Elsethagen T, Sun L, Gurumoorthi V, Chase J, Li J, Windus TL (2007) Basis set exchange: a community database for computational sciences. J Chem Inf Model 47:1045-1052. https://doi.org/10.1021/ci600510j
21. Zhao Y, Truhlar DG (2008) Computational characterization and modeling of buckyball tweezers: density functional study of concave-convex π···π interactions. Phys Chem Chem Phys 10:2813-2818. https://doi.org/10.1039/b717744e
22. Grimme S (2012) Supramolecular binding thermodynamics by dispersion-corrected density functional theory. Chemistry 18:9955-9964. https://doi.org/10.1002/chem.201200497
23. Mennucci B, Tomasi J, Cammi R, Cheeseman JR, Frisch MJ, Devlin FJ, Gabriel S, Stephens PJ (2002) Polarizable Continuum Model (PCM) Calculations of Solvent Effects on Optical Rotations of Chiral Molecules. J Phys Chem A 106:6102-6113. https://doi.org/10.1021/jp020124t
24. Minenkov Y, Occhipinti G, Jensen VR (2013) Complete Reaction Pathway of Ruthenium-Catalyzed Olefin Metathesis of Ethyl Vinyl Ether: Kinetics and Mechanistic Insight from DFT. Organometallics 32:2099-2111. https://doi.org/10.1021/om301192a
25. Sperger T, Sanhueza IA, Kalvet I, Schoenebeck F (2015) Computational Studies of Synthetically Relevant Homogeneous Organometallic Catalysis Involving Ni, Pd, Ir, and Rh: An Overview of Commonly Employed DFT Methods and Mechanistic Insights. Chem Rev 115:9532-9586. https://doi.org/10.1021/acs.chemrev.5b00163
26. Grandner JM, Shao H, Grubbs RH, Liu P, Houk KN (2017) Origins of the Stereoretentive Mechanism of Olefin Metathesis with Ru-Dithiolate Catalysts. J Org Chem 82:10595-10600. https://doi.org/10.1021/acs.joc.7b02129
27. Janse van Rensburg W, Steynberg PJ, Meyer WH, Kirk MM, Forman GS (2004) DFT prediction and experimental observation of substrate-induced catalyst decomposition in ruthenium-catalyzed olefin metathesis. J Am Chem Soc 126:14332-14333. https://doi.org/10.1021/ja0453174

28. Romero PE, Piers WE (2007) Mechanistic studies on 14-electron ruthenacyclobutanes: degenerate exchange with free ethylene. J Am Chem Soc 129:1698-1704. https://doi.org/10.1021/ja0675245
29. Mikus MS, Torker S, Hoveyda AH (2016) Controllable ROMP Tacticity by Harnessing the Fluxionality of Stereogenic-at-Ruthenium Complexes. Angew Chem Int Ed Engl 55:4997-5002. https://doi.org/10.1002/anie.201601004